Fachhochschule Aachen

Campus Jülich

Fachbereich 10: Energietechnik

Physical Engineering

Low temperature powder diffraction studies on ternary chalcogenides

Angefertigt am
Jülich Centre for Neutron Science, JCNS-2,
Und Peter Grünberg Institut,PGI-4:
Streumethoden
Forschungszentrum Jülich GmbH

Bachelorarbeit von Zikang Li

Jülich, Mai, 2017

Diese Arbeit wurde betreut von:

1. Prüfer: Prof. Dr. rer. nat. Arnold Förster
2. Prüfer: PD Dr. Karen Friese

Betreuer: Markus Herrmann

Diese Arbeit ist von mir selbständig angefertigt und verfasst. Es sind keine anderen als die angegebenen Quellen und Hilfsmittel benutzt worden.

_____   _____

Ort, Datum   eigenhändige Unterschrift

Table of contents

List of figures

List of tables

List of abbreviations

Å	$10^{-10}\ m$
Bi	Bismuth
Et	$-Ch_2Ch_3$
N	Nitrogen
P	Phosphorus
Ph	Phenyl group
Pr	$-Ch(Ch_3)_2$
Sb	Antimony
Se	Selenium
Te	Tellurium

1.Introduction

Topological insulators e. g. Sb_2Te_3 and Sb_2Se_3 belong to the group of narrow gap semiconductors ($Eg < 1\,eV$) and have attracted a lot of attentions over the last decades due to their thermoelectric properties [1]. Materials for thermoelectric applications are characterized by a large figure of merit ZT = $\sigma S^2 T/\kappa$ with the electrical conductivity σ, the Seebeck coefficient S and the thermal conductivity κ [2]. It has been shown in previous studies that binary pnictide chalcogenides e. g. $Sb_2Se_{3-x}Te_x$ as well as related compounds, are suitable candidates for thermoelectric applications. Furthermore, these materials have been investigated as materials for reversible memory switching applications [1].

The crystal structures of the endmembers, Sb_2Te_3 and Sb_2Se_3, have been studied intensively in the past [2,3]. In table 1 the lattice parameters of Sb_2Te_3 published in previous studies are summarized [1,2,4]. Sb_2Te_3 crystallizes in the space group R-3m with Z=3. The crystal structure of Sb_2Te_3 is shown in figure 1. The unit cell is given in the hexagonal setting. The structure is formed by repeated stacking of quintuple layers of "-[Te2-Sb-Te1-Sb-Te2]-"units along the c-axis. Within the structure 2 types of differently bonded tellurium atoms (Te1; Te2) exist [2]. The Te1 atoms are coordinated by 6 Sb atoms from neighboring layers in the form of a distorted octahedron. The Te2 atoms are coordinated by only three Sb atoms. In addition, each Te2 atom is coordinated by three Te2 atoms through Te2…Te2 van der Waals interactions Mansour, et al. [2]. Therefore, the octahedral around Te2 show a significantly stronger distortion [2]. The low temperature behavior of Sb_2Te_3 was investigated between 10 to 298 K by neutron and X-ray powder diffraction and heat capacity measurements. No phase transitions were found in this temperature range [2].
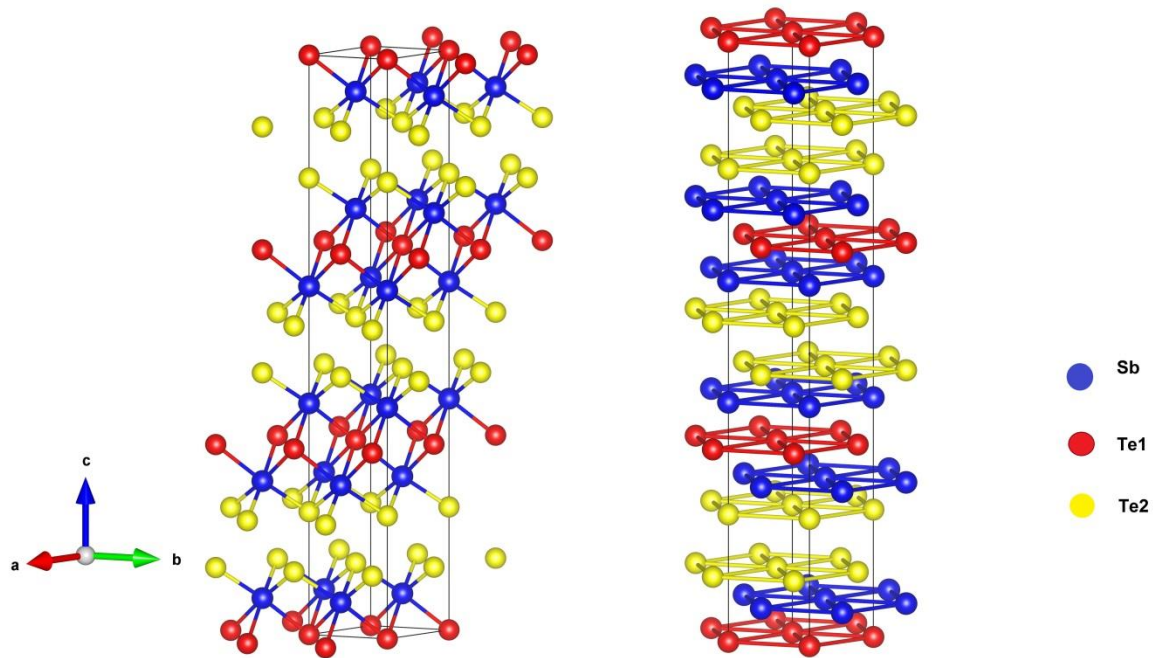
Figure 1: Crystal structure of Sb$_2$Te$_3$

Reference	Temperature	Lattice parameter a/ Å	Lattice parameter c/ Å	Lattice parameter V/Å^3
[1]	50K	4.2485	30.275	473.23
	280K	4.2636	30.430	479.04
[2]	10K	4.2547(3)	30.268(3)	474.53(9)
	298K	4.2674(7)	30.450(3)	480.23(9)
[4]	10K	4.2423	30.191	470.54
	270K	4.2537	30.288	474.82

Table 1: Established studies of lattice parameter of Sb$_2$Te$_3$

Sb_2Se_3 crystallizes in the orthorhombic space group Pnma with Z=4 and lattice parameter of *a*=11.7938(9), *b*=3.9858(6), *c*=11.6478(7) Å at room temperature [3]. The structure of Sb_2Se_3 is formed by "infinite chains" along the direction of the b-axis and is shown in Figure 2.
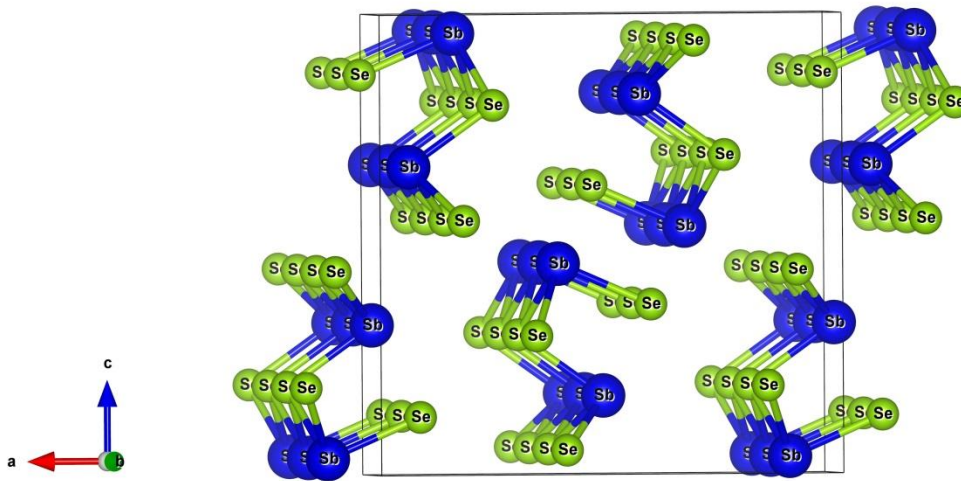
Figure 2: Crystal Structure of Sb_2Se_3

Figure 3 shows the phase diagram of the Sb_2Se_3-Sb_2Te_3 solid solution[5]. While the crystal structure of Sb_2Te_3 is stable for Te contents between 40-100 mole %, orthorhombic mixed crystals, which are isostructural to Sb_2Se_3, are formed for Te contents of about 0-5 mole %. For Te contents of 5-40 mole % a two phase region was observed. Molodkin *et al*. [6] have performed measurements of X-ray powder diffraction, the Seebeck coefficient, thermal conductivity and electrical conductivity from 50 to 500 ℃ on some $Sb_2Se_{3-x}Te_x$ mixed crystals. For the composition Sb_2SeTe_2 they observed a pronounced maximum of thermal and electrical conductivity, also a pronounced minimum of Seebeck coefficient. Together with the change in the lattice parameters, they attributed this to the existence of a phase with an ordered contribution of Se and Te. Up to now, the low temperature behavior of the $Sb_2Se_{3-x}Te_x$ mixed crystals is unkown. However, E*. P.* Amaladass *et. Al* [7]have investigated different compounds from the $Bi_2Se_{3-x}Te_x$ solid solution, which are isostructural to the structure type of Sb_2Te_3, by magneto-resistance measurements and X-ray diffraction between 4 to 300 K and no phase transitions were detected in this temperature range.
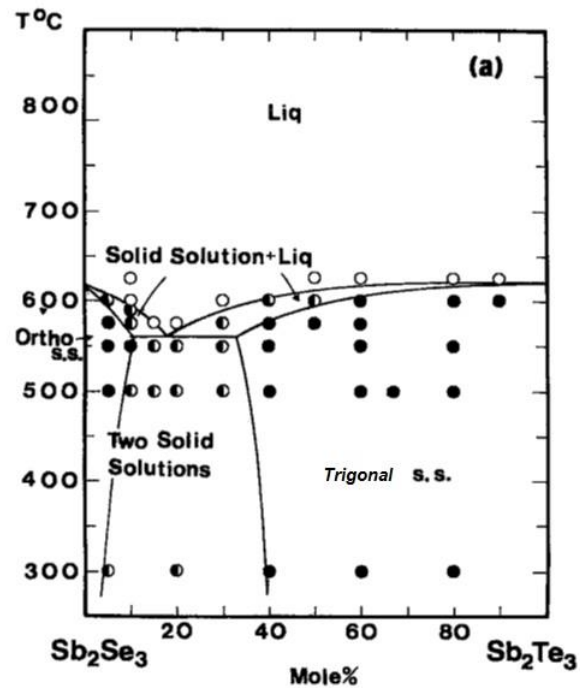
Figure 3: Phase diagram of Sb$_2$Se$_{3-x}$Te$_x$ solid solution [5]

Polycrystalline material of the end members, Sb$_2$Te$_3$ and Sb$_2$Se$_3$, as well as of $Sb_2Se_{3-x}Te_x$ mixed crystals were synthesized by different methods, from which the most important ones are summarized in Table 2:

No.	Staring material	Product(s)	Temperature	Atmosphere	Time	Cool down	Reference
1	Sb, Te (95 %)	Sb_2Te_3	675 °C	Step 1: vacuum Step 2: Ar; 0.8 mbar	-	Slow cooling	[1]
2	Sb,Te(5N)	Sb_2Te_3	900 °C	vacuum ; $< 10^{-7}$ Torr	-	Slow cooling	[4]
3	Sb, Se, Te (5N)	$Sb_2Se_{3-x}Te_x$	700 °C	evacuated	>24 h	Slow cooling	[8]
4	$Sb_2Te_3 + Sb_2Se_3$(5N)	$Sb_2Se_{3-x}Te_x$	Step 1: 800°C Step 2: 730°C	evacuated	Step 1: 48 h Step 2: 24 h	Slow cooling	[9]
5	$Sb[(TeP^iPr_2)_2N]_3$ (P^i=Phosphate groups)	Sb_2Te_3	375-475°C	evacuated	1 h 10 min	Slow cooling	[10]
6	Ph_3SbTeR (R=Et, Ph)	Sb_2Te_3	Step 1: 90 °C Step 2: 300 °C	evacuated	Step 1: 1 h Step 2: 2 h	Slow cooling	[11]
7	Sb, Se (5N)	Sb_2Se_3	900 °C	evacuated	2 h	Slow cooling	[12]

Table 2: Different synthesizing methods of Sb$_2$Se$_{3-x}$Te$_x$powder samples

Synthesis of Sb_2Te_3 and Sb_2Se_3 were performed from stoichiometrically weighted amounts of the elements Sb and Se/Te [8,12]. The heat capacity of Sb_2Se_3 was studied by A.S.Pashinkin *et. al* [12]

between 53 K to 600 K by differential scanning calorimetry and no anomalies have been observed in this temperature range. The synthesis is possible in a wide temperature range (675-900 °C) and on timescales from less than one day to more than two days. Furthermore, synthesis of Sb_2Te_3 and Sb_2Se_3 were performed in evacuated ampoules as well as under Ar atmosphere [9]. Synthesis of nano-crystalline Sb_2Te_3 was performed from Single-Source Percursor methods [10], which can be performed below the melting point of Selenium (494 K) and Antimony(903.8 K) [13]. Synthesis of $Sb_2Se_{3-x}Te_x$ were carried out from stoichiometrically weighted amounts of the endmembers, Sb_2Te_3-Sb_2Se_3 and from elements, respectively. D.P.Gosain *et al.* [9] have determined melting points of about 410 °C for some mixed crystals in the stability field of the trigonal phase. The melting points of the endmembers Sb_2Te_3 and Sb_2Se_3 are 902 K and 884 K, respectively.

This BSc thesis is focused on the synthesis of $Sb_2Se_{3-x}Te_x$ mixed crystals (x=0, 0.6, 1.2, 1.8, 3) and the determination of the temperature dependencies of the lattice parameters of these compounds by low temperature X-ray powder diffraction (LTXRPD). The $Sb_2Se_{3-x}Te_x$ mixed crystals were synthesized by melting of the individual elements *Sb, Se, Te* (5N). The LTXRPD measurements were carried out in the temperature range between 20 and 300 K. The aims of this study are to find suitable reaction conditions for the synthesis of stoichiometric $Sb_2Se_{3-x}Te_x$ mixed crystals and to improve the understanding of the low temperature behavior of the lattice parameters of these compounds.

2. Theory

2.1 Basics of crystal lattices and diffraction

2.1.1 Lattice planes in crystals

A crystal is formed from an ordered, periodic arrangement of atoms, molecules, or ions. Crystal lattices are characterized by translational symmetry with the unit cell as the smallest repeat unit. The dimension of the unit cell is described by the lattice parameter (*a,b,c*) and the angles between them (*α,β,γ*)[14]. In a crystal all parallel lattice planes contain the same translationally equivalent arrangements of atoms. The different lattice planes are described by their Miller Indices *hkl.* The distance between two neighboring lattice planes is defined by the *d*-spacing (e.g. d_1, d_2, d_3 (Figure 4)).
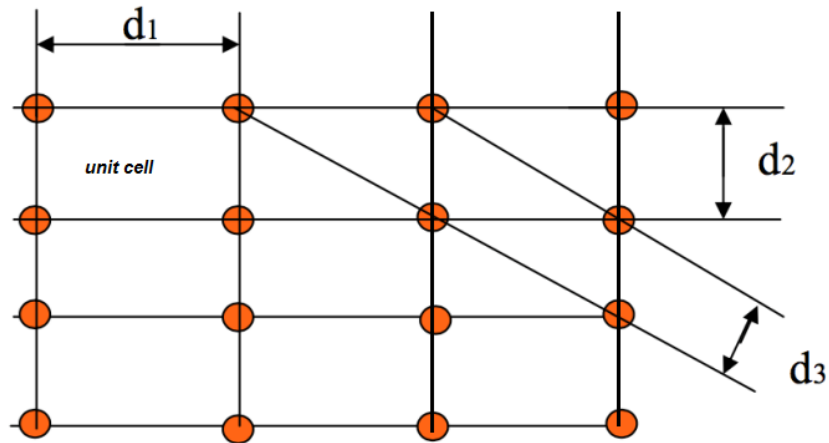
Figure 4: Illustration of a 2-dimensional crystal lattice. A unit cell is indicated and d-spacings of different lattice planes are shown

2.1.2 X-ray scattering and Bragg´s law

When a focused X-ray beam interacts with atoms in a crystal, a part of the beam is transmitted, a part is absorbed by the sample, and a part is scattered. The wavelength of the x-ray beam is comparable to the *d*-spacings in the periodic crystal lattice and the x-ray beam can thus be scattered by the crystal. Diffraction only occurs when the different scattered beams show constructive interference and the amplitude of the resulting wave is increased (Figure 5). Destructive interference of the waves leads to vanishing amplitudes of the resulting wave.

The Bragg Equation describes the condition for constructive interference of two waves which are scattered by neighboring lattice planes in a crystal as a function of the incoming angle $\boldsymbol{\theta}$.
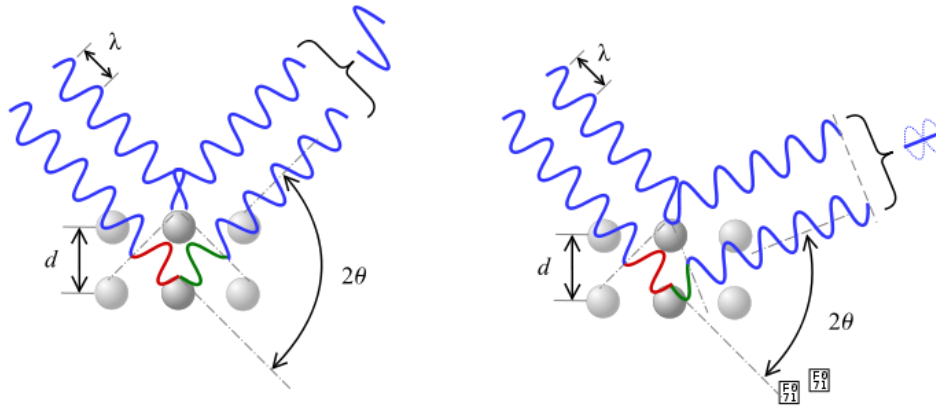
Figure 5: Constructive interference (left) destructive interference (right) [15]

When the atoms on a lattice plane are hit by an incoming beam under an angle $\boldsymbol{\theta}$, the diffracted beam will also come out at the same angle $\boldsymbol{\theta}$ (Figure 6). Therefore, the overall angle after diffraction is $\boldsymbol{2\theta}$.
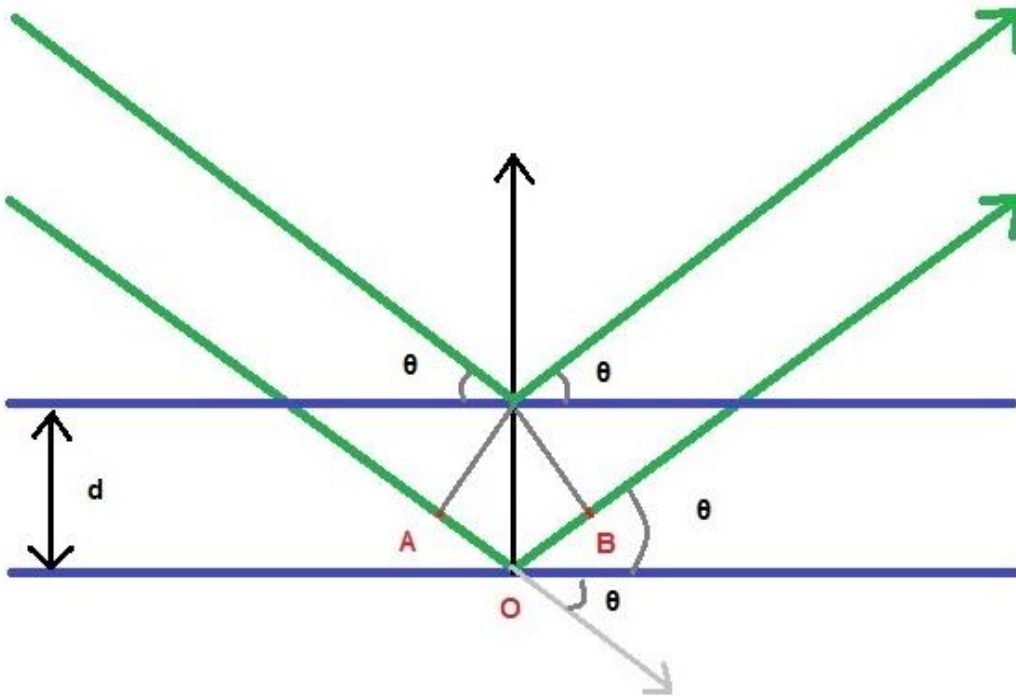
Figure 6: Illustration of Bragg's law. Incident and scattered waves are indicated.

Figure 6 shows two parallel beams, which are scattered on two neighboring lattice planes. The path difference between the beams is given by:

$$\Delta = AO + BO \qquad (1)$$

and

$$d \cdot \sin\theta = AO = BO \qquad (1)$$

Constructive interference between the waves scattered by the two lattice planes can only occur if

$$n\lambda = \Delta \qquad (3)$$

A combination of the equations (1,2,and 3) yields Bragg´s equation, which is given by

$$n \cdot \lambda = 2d \cdot \sin\theta \qquad (4)$$

where n is a positive integer, which describes the order of diffraction.

The relationship between the spacing d of the lattice planes and d_{hkl} is given by $d = d_{hkl} \cdot n$. With this one can also write:

$$\lambda = 2 \cdot d_{hkl} \cdot \sin \theta \qquad\qquad (5)$$

2.2 d_{hkl} and lattice parameter

In powder diffraction experiments the angle 2θ under which constructive interference occurs will be measured. From this the spacing of the lattice plane's d_{hkl} can be determined using Bragg´s law and the lattice parameters which define the dimensions of the unit cell can be deduced.

While a crystal lattice is described in real space, a diffraction experiment is described with the help of a reciprocal lattice (see Figure 7) which is defined by following equations:

$$a^* = \frac{bc \cdot \sin\alpha}{V}, b^* = \frac{ac \cdot \sin\beta}{V}, c^* = \frac{ab \cdot \sin\gamma}{V}$$

$$\alpha^* = \arccos[(\cos\beta \cdot \cos\gamma - \cos\alpha)/(\sin\beta \cdot \cos\gamma)]$$

$$\beta^* = \arccos[(\cos\alpha \cdot \cos\gamma - \cos\beta)/(\sin\alpha \cdot \cos\gamma)]$$

$$\gamma^* = \arccos[(\cos\alpha \cdot \cos\beta - \cos\gamma)/(\sin\alpha \cdot \sin\beta)]$$
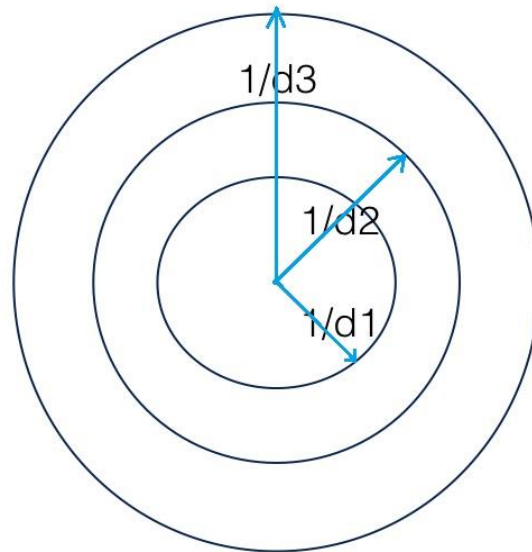
Figure 7: Rings of radius d*$_{hkl}$ as formed in a powder diffraction diagram

Furthermore,

$$\left|\overrightarrow{\mathbf{d^*_{hkl}}}\right|^2 = \frac{1}{\mathbf{d^2_{hkl}}} \qquad (6)$$

The value of $d^*_{hkl}{}^2$ is then given by

$$\mathrm{d^*_{hkl}}{}^2 = h^2 \cdot a^{*2} + k^2 \cdot b^{*2} + l^2 \cdot c^{*2} + 2hk \cdot a^*b^*cos\gamma^* + 2hl \cdot a^*c^*cos\beta^* + 2kl \cdot b^*c^*cos\alpha^* \quad (7)$$

Due to the geometry in a powder diffraction experiment, different rings with radius r are recorded for each value of d^*_{hkl} which can be directly related to the lattice parameter and d-spacings of the crystal using equations 6 and 7 In the actual experiment, the powder crystallites have all possible orientations, so the summary of each diffraction angle 2θ will be like a cone (Figure 8). For every crystalline material the diffraction angles $2\theta_i$ and the different cones are specific.
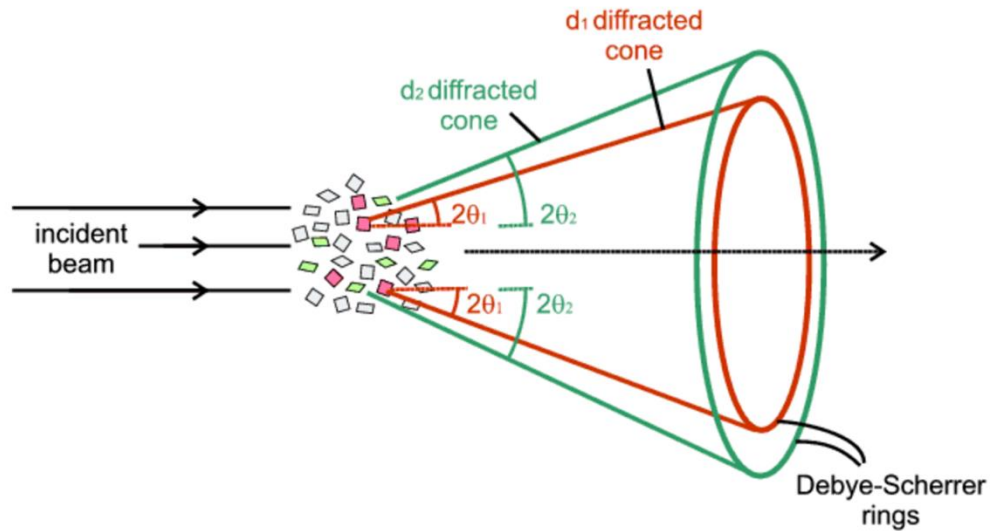
Figure 8: : Schematic drawing of the diffracted cones originating from the powder crystallites [16]

The samples which were investigated in the course of this thesis belong to different crystal systems. Sb_2Se_3 belongs to the orthorhombic system, where $\alpha = \beta = \gamma = 90°$; $a \neq b \neq c$ and $Sb_2Se_{3-x}Te_x$ (x=0.6; 1.2; 1.8) belongs to the trigonal system where $\alpha = \beta = 90°; \gamma = 120°; a = b \neq c$. For these systems the lattice spacing d_{hkl} can be obtained with:

Orthorhombic system:

$$d_{hkl} = \frac{1}{\sqrt{(\frac{h}{a})^2 + (\frac{k}{b})^2 + (\frac{l}{c})^2}}$$

Trigonal system:

$$d_{hkl} = \frac{1}{\sqrt{\left(\frac{h^2 + hk + k^2}{a^2}\right) + \frac{3}{4}(\frac{l}{c})^2}}$$

2.3 Powder Diffractometer

Figure 2.3 shows a schematic drawing of a Powder diffractometer, which is used in transmission geometry. The diffractometer is equipped with an X-ray tube, a monochromator, a divergence slit located between the X-ray source and the sample, and a detector[17]. In addition, the diffractometer can be equipped with a low temperature system. In the following chapters the different components of the powder diffractometer will be discussed in more detail.
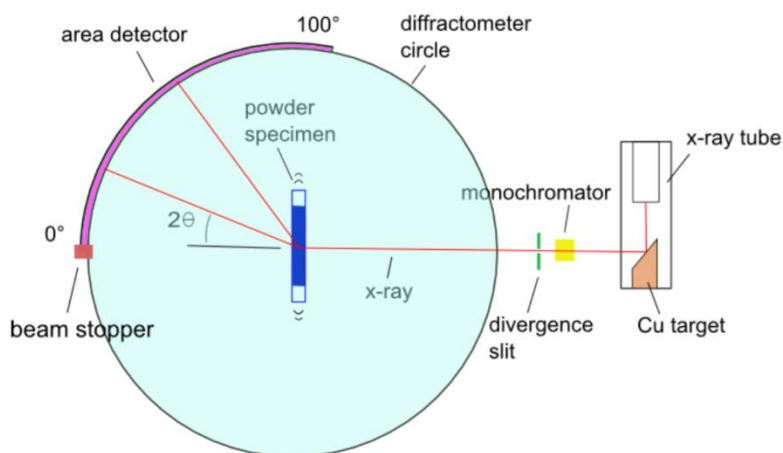
Figure 9: Schematic drawing of the setup of a powder diffractometer [17].
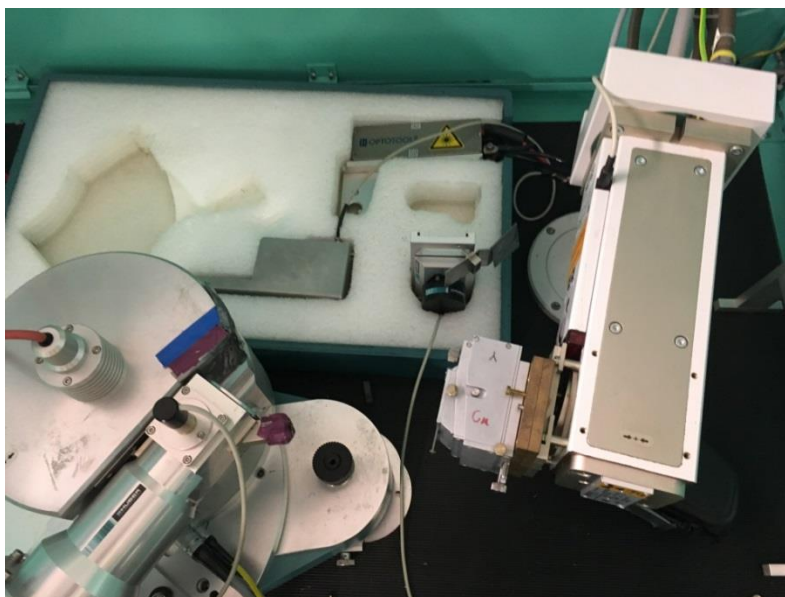
Figure 10: Photo of the Huber diffractometer used in this work

2.3.1 Generation of x-rays

The ground state of an atom is defined by a nucleus surrounded by different orbits which are occupied by the electrons according to *Bohr model*. The orbits are labelled alphabetically as *k,l,m,n* where *k* corresponds to the orbit closest to the nucleus.
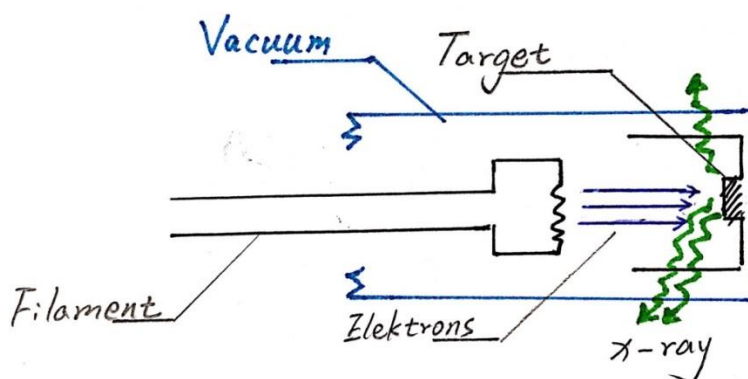
Figure 11: Schematic representation of an X-ray generator

X-rays are generated by heating a filament, this way producing free electrons. Figure 11 shows a scheme of an x-ray generator. A high voltage is applied to accelerate these electrons towards a metal target. The accelerated electrons knock an electron out of the inner shell of an atom of the metal target, resulting in an excited nuclear state. Electrons from higher electron shells fall down to the lower level and occupy the   vacancy in the inner shell. This is accompanied by an emission of X-rays with wavelengths ranging from 0.01 to 10 nm depending on the target material. Each element has a unique set of energy levels, and thus the transition from higher to lower energy levels produces X-rays with frequencies that are characteristic to each element. If an electron falls from the *l* shell to the *k* shell, the emitted radiation is called *Kα*. Similarly, when an electron falls from the *m* shell to the *k* shell, the emitted radiation is called *Kβ*. Figure 12 shows the characteristic emission spectrum of Copper.
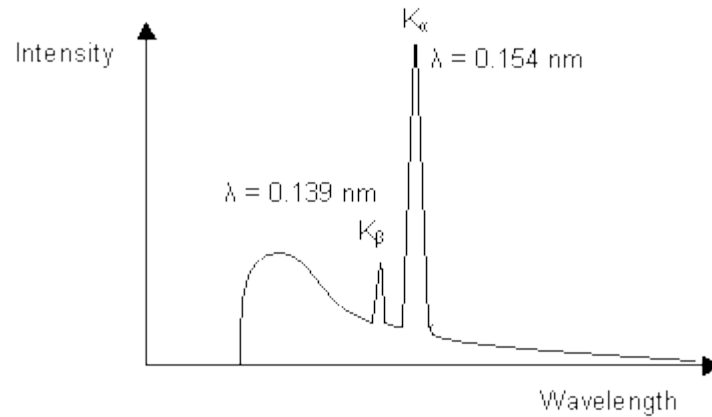
Figure 12: Characteristic emission spectrum of Copper[18]

In the powder diffraction experiments performed here the used target material was copper with a wavelength corresponding to CuKα-radiation (average $\lambda = 0.154\ nm$).

2.3.2 Monochromator

Between the x-ray tube and the sample a soller slit and a monochromator are placed. X-ray monochromators are used to select only radiation of the desired wavelength from the X-ray source. For this, Bragg diffraction on a suitable single crystal is used. Only the wavelengths for which the Bragg condition is fulfilled under a certain angle ϑ are selected. For a silicon crystal which is cubic with an *a* lattice parameter of 0.54309 nm, the largest *d* spacing which originates from the (111) planes is 0.3136 nm. Application of the Bragg equation ($\lambda = 2d_{hkl}\ sin\vartheta$) shows that for CuKα radiation, the diffraction condition will be satisfied for *2ϑ* = 28.427 °, for CuKβ, it will be satisfied for 2θ= 25.608°, resulting in a difference in the Bragg angle of 2.819 °. With the help of the monochromator it is thus possible to select the Kα wavelength from the laboratory copper X-ray source. The divergence slits in front of the sample are used to limit the divergence of the incoming x-ray beam.

2.3.3 Detector of diffractometer

An imaging plate detector system is used as 2-dimensional detector on the Huber diffractometer (Figure 13). The image plate on the Guinier camera 670 is situated on the focal circle with the photon sensitive side facing inwards. During one exposition the Bragg angle is recorded and scanned in the range from 0-100° with a step size of 0.005 °.
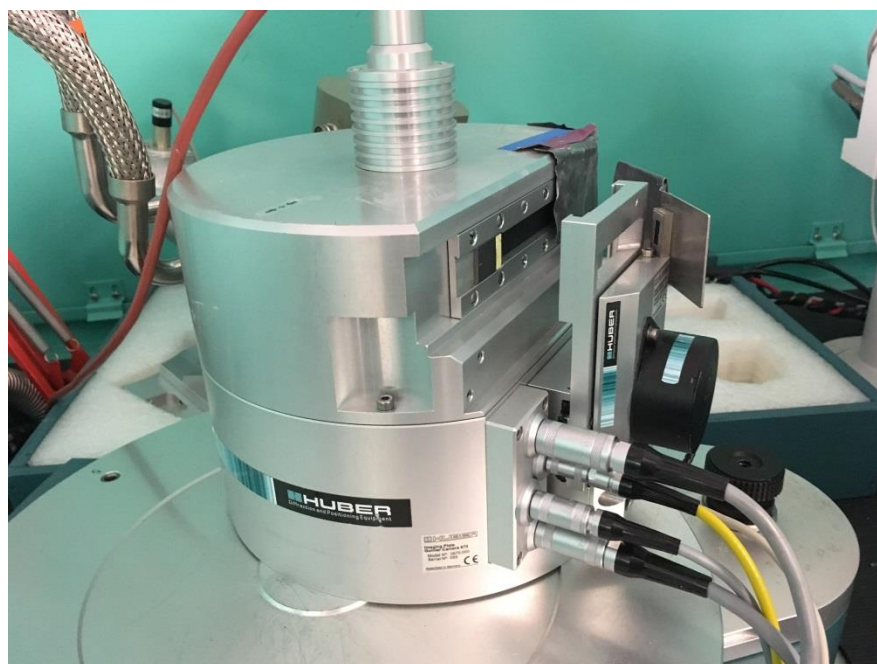
Figure 13: Photo of Image plate detector system of the Huber diffractometer with housing

Therefore, a complete diffractogram consists of maximum 20001 measurement points. Inside the detector housing, a laser recording unit with a photomultiplier and preamplifier and a halogen lamp are also located. After the imaging plate is exposed to the X-rays, the image plate is scanned by a vertical linear red diode laser beam within approximately 5 seconds. During the scanning process, the blue photostimulated luminescence is excited from the areas which have been subjected to X-ray exposure. The obtained signal is amplified by the photomultiplier tube, digitized by a 16-bit A/D-converter and then transferred to the control computer. The halogen lamp is then used to delete the information recorded on the imaging plate. After this process the Guinier camera is ready for recording the next image.

2.3.4 Cryostat

The powder diffractometer is combined with a cryostat which provides the desired temperature for the measurement (see Figure 14). Inside the cryostat chamber, the sample is enclosed in a Cu block, which is surrounded by two cooling shields. In addition, the cooling head incorporates a heating element and Si-diodes as temperature sensing elements are connected for temperature regulation.
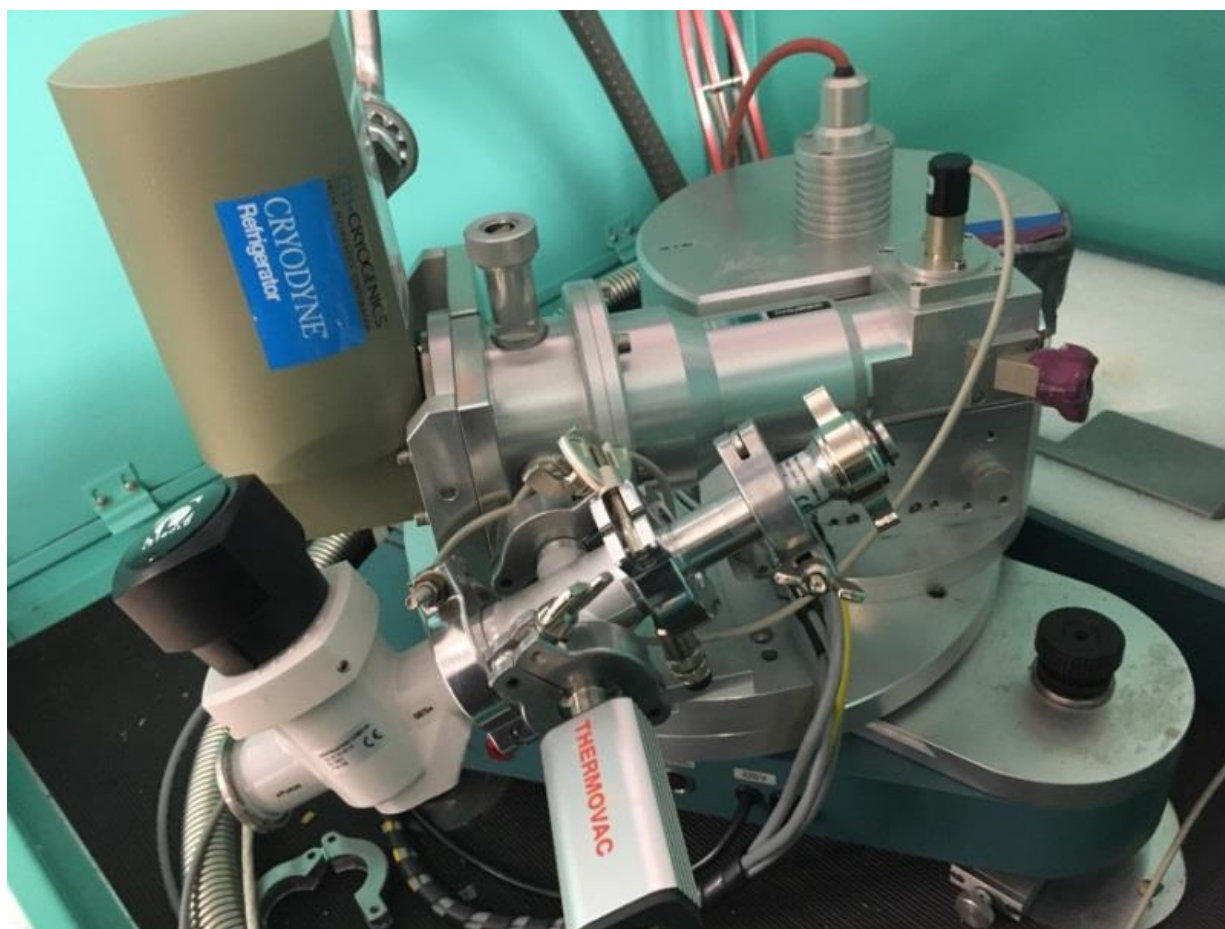
Figure 14: Photo of chamber and cooling system of cryostat

The closed cycle Helium cooling System is supplied by an air-cooled compressor. The regulating system is controlled by a computer (Figure 15). Powder samples covered with foils can be investigaed at temperatures between approximately 12 K to 350 K. For this, the sample is inserted into the chamber and an electric motor is switched on to keep it moving back and forth.

Figure 15: Photo of the Cryostat Controller Unit

3. Experimental details

3.1 Synthesis Sb$_2$Se$_{3-x}$Te$_x$ of mixed crystals

Synthesis of powder samples of $Sb_2Se_{3-x}Te_x$ (x=0.6; 1.2; 1.8; 3) were performed according to the reaction equation:

$$2Sb + (3-x)Se + xTe \xrightarrow{\sim 948K;0.8bar;Ar} Sb_2Se_{3-x}Te_x$$
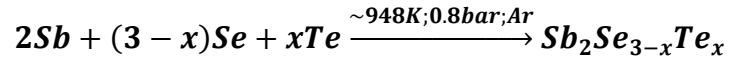
Pure Sb(5N;pieces;ChemPUR), Te(5N;pieces;PreussAG), Se(5N;granuless;ChemPUR) elements were weighed in the respective mass ratio of the compounds ($Sb_2Se_{3-x}Te_x$ (x=0.6; 1.2; 1.8; 3) as shown in the attachment [Table A].

The starting materials were filled into crucibles and the crucibles were placed in Quartz-glass ampoules. On the top of each crucible a Quartz-glass plug was placed (Figure 16 and 17). The ampoules were evacuated (p=10^-5 bar) and Ar atmospheres of 0.8 bar were adjusted. The reactions were performed using the temperature profile portrayed in Figure 18. After the reactions the products were cooled slowly by switching of the furnace. In order to reduce the Se and Te escape during the reactions as much as possible, different crucible shapes and the B_2O_3 liquid encapsulation method were tested.

Table 3 shows three different kinds of synthesis variants A, B and C that were used:

Variant A)	Aluminum oxide crucible; flat bottom; approx. r=1.6cm inner radius
Variant B)	Quartz glass crucible; sharp bottom; approx. r=0.5cm inner radius
Variant C)	Quartz glass crucible; sharp bottom; approx. r=0.5cm inner radius; covered with Boron trioxide(B_2O_3) between glass plug and elements

Table 3: Three different kinds of synthesis variants A, B and C in this experiment

Figure 16: Synthesis variant A. The tubes contain the sample before the melting process.
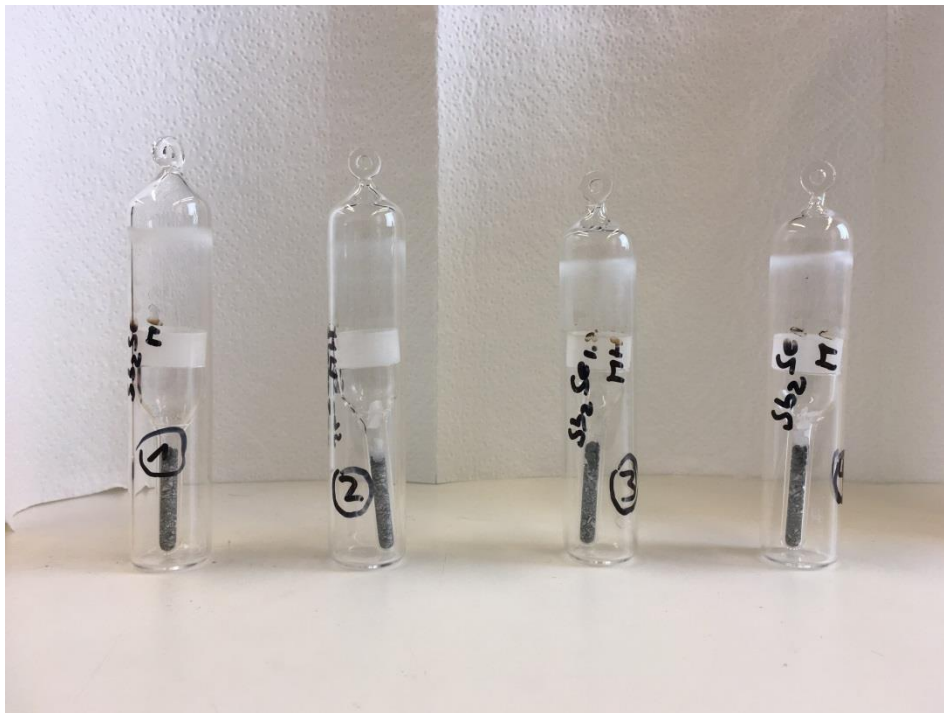
Figure 17: Synthesis variant B and C. Tubes contain the sample before the melting process.
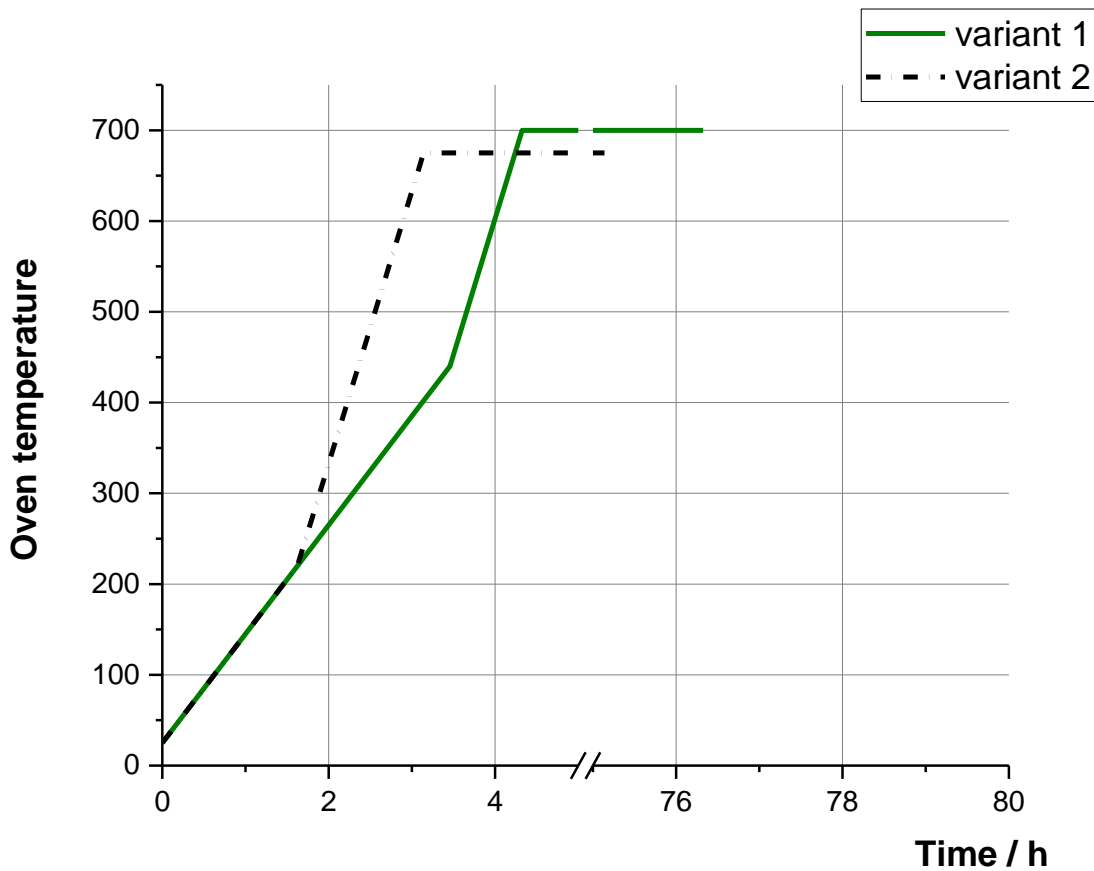
Figure 18: Temperature profile for the synthesis. (Variant 1: heating speed 2 k/min from 25 °C to 220; 5 k/min from 220 °C to 675 °C; keep 675 °C for 72 h; Variant 2: heating speed 2 k/ min from 25°C to 440; 5 k/ min from 440 °C to 700 °C (only Sb_2Te_3); keep 700 °C for 72 h)

After cooling down of the samples, a hammer was used to break off the tube and to get the resulting ingot. To get a smooth and regular distribution of crystal orientations and to avoid a preferred orientation effects in the powder diffraction experiment, the grains inside the powder should be in the range of 1-50 microns. The synthesized ingots were thus crushed into smaller pieces and grinded further with a mortar until this requirement was fulfilled. In the end the samples were weighed and the yields of the syntheses were measured (Table 4).

Variant	Sb_2Te_3	$Sb_2Se_{0.6}Te_{2.4}$	$Sb_2Se_{1.2}Te_{1.8}$	$Sb_2Se_{1.8}Te_{1.2}$	$Sb_2Se_{2.4}Te_{0.6}$	Sb_2Se_3
A	99.4 %	94 %	98 %	99.5 %	99.16 %	98.3 %
B	-	99 %	99.6 %	-	-	-
C		Over 100 %	Over 100 %			

Table 4: Yields of the synthesis

3.2 Measure powder samples

A suitable amount of powder sample was put between two caption foil and the sample carrier was set in front of the detector vertically. To avoid the sample from falling down due to gravity, isopropanol or vaseline was used to attach the powder on the foil. Before the low temperature measurement was started a test measurement at room temperature was performed. For this the measurement time was set to 10 minutes and the resulting diffractogram was checked for a satisfactory quality. For the low temperature measurement the sample was placed on the special low temperature sample holder. The smaple holder was then introduced into the cryostat and the vacuum pump was opened. Then the desired temperature profile was set on the computer (Table 5) and the measurement was started. The measurement program was identical for all measured samples.

Temperature start	20 K
Temperature end	300 K
Step	5 K
Measure time	120 min
Dwell time	5 K/ min

Table 5: Measurement program for the low temperature powder diffraction measurements

3.3 The Le Bail Method [14]

The knowledge of well-defined lattice parameters is an important topic in many research areas. The LeBail refinement [19] is a key method to determine the lattice parameter of polycrystalline compounds. The Le Bail Method (Figure 19) is an iterative method and ideally suited to follow the change in lattice parameter as a function of thermodynamic variables like e.g. temperature or pressure. The underlying algorithm has been introduced into many programs which performrefinement of powder diffraction data.

Initial a, b, c, α, β, γ + Spacegroup

Initial 2θk

Calculated Iobs

Use new data ## Set I(calc)=I(obs)

Least-squares-fit

New a, b, c, α, β, γ
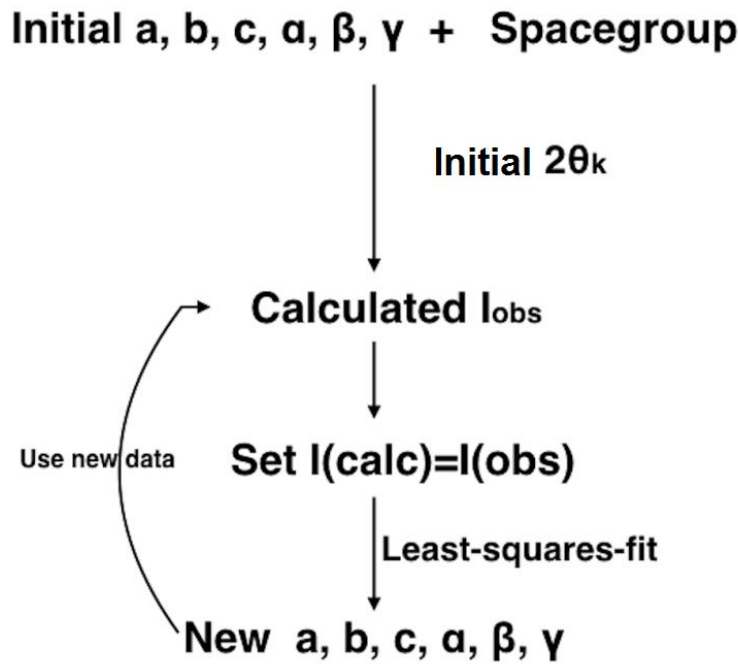
Figure 19: Illustration of the 'Le Bail process'

For the application of the Le Bail method, pre-determined approximate lattice parameter, either from a structural model provided in the literature or deduced from indexing of the powder data, must be available. Ideally the space group of the crystal is also known. The lattice parameter in combination with the space group symmetry, define all possible $2\theta_k$ positions of reflections in a powder diffraction diagram.

The intensities for each point $2\theta_{ki}$ of the diffractogram of a single phase is given by

$$y_i(calc) = \sum_k I_k \cdot G(2\theta_i - 2\theta_k) + b_{ig} \qquad (1)$$

using arbitrary starting values $y_i(i)$. In equation (1), I_k are the calculated intensities, $G(2\theta_i - 2\theta_k)$ is the profile function, and b_{ig} is the background function.

In the LeBail refinement, the difference $\Delta = \sum wi\,(y_{obs} - y_{calc})^2$ with weighting factor $wi = \dfrac{1}{y_{i,obs}}$ is minimized by a least-squares method. Here (y_{calc}) is the calculated and (y_{obs}) is the observed intensity

Initially the intensities (y_{calc}) are set to arbitrary values. If two (or more) reflections overlap, then

$$I(1)_{obs} = \Sigma_i \frac{y_i(obs) \cdot y_i(1)}{y_i(calc)} \quad ; \quad I(2)_{obs} = \Sigma_i \frac{y_i(obs) \cdot y_i(2)}{y_i(calc)} \qquad (2)$$

And the total intensity at a point y_i is given by :

$$y_i(calc) = y_i(1) + y_i(2) \qquad (3)$$

Figure 20 illustrates how the calculated (y_{calc}) and observed (y_{obs}) intensities are minimized. The calculated (y_{calc}) intensity is a summation of $y_i(1)$ and $y_i(2)$ taking into account the shape and asymmetry of the observed (y_{obs}) intensities.
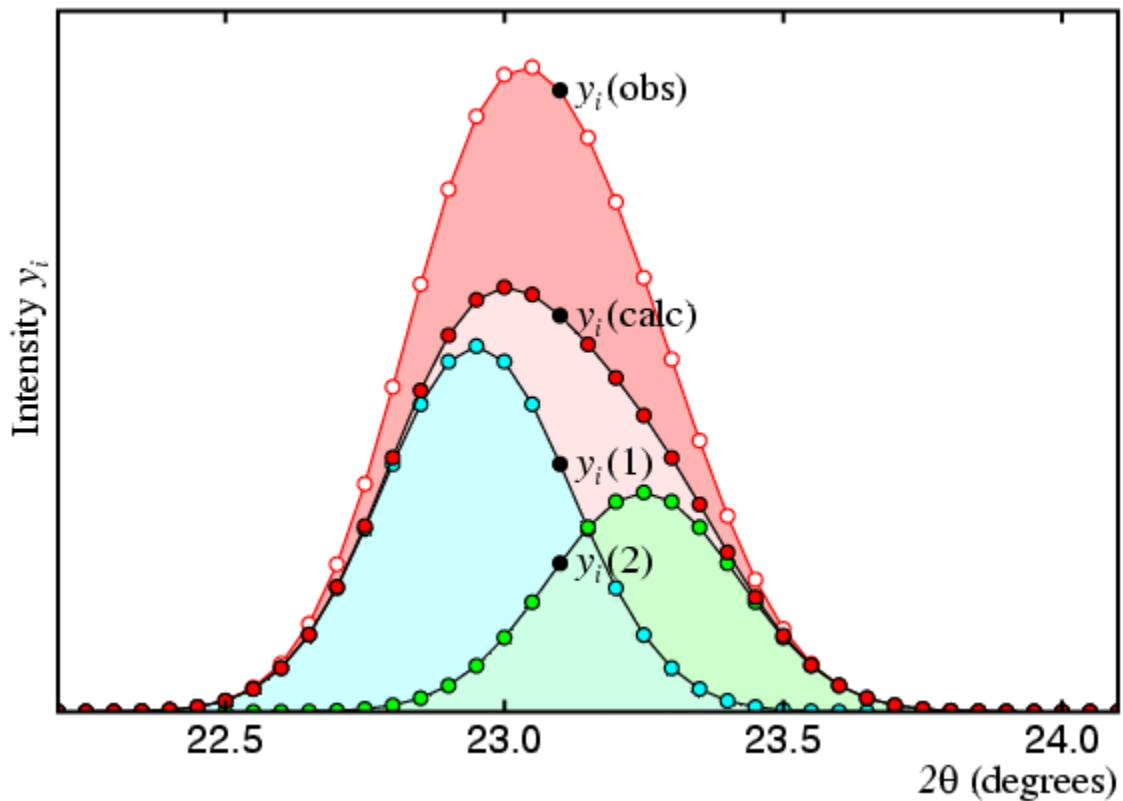
Figure 20: Fitting with the Lebail Method [15]

The profile function $G(2\theta_i - 2\theta_k)$ describes the shapes of the observed peaks. In practice a Pseudo-Voigt function pV is used often. This function contains a Lorentzian part and a Gaussian part:

$$pV = \mu \cdot \left(\frac{\sqrt{4}}{\pi \cdot H_{k,Lorentzian}}\right) \cdot \left(\frac{1}{1+4\cdot(x_{ik})^2}\right) + (1-\mu) \cdot \left(\frac{\sqrt{4\cdot ln2}}{\sqrt{\pi}\cdot H_{k,gaussian}}\right) \cdot (\exp(-4 \cdot ln2 \cdot (X_{ik}))) \qquad (4)$$

With the Lorentzian part: $\quad \mu \cdot \left(\frac{\sqrt{4}}{\pi \cdot H_{k,Lorentzian}}\right) \cdot \left(\frac{1}{1+4\cdot(x_{ik})^2}\right) \qquad (5)$

$$H_{k,Lorentzian} = LX \cdot tan\theta + \frac{LY}{cos\theta} \qquad (6)$$

$$LX = \frac{1800 \cdot K \cdot \lambda}{D \cdot \pi} \qquad (7)$$

And the Gaussian part: $\quad (1-\mu) \cdot \left(\frac{\sqrt{4\cdot ln2}}{\sqrt{\pi}\cdot H_{k,gaussian}}\right) \cdot (\exp(-4 \cdot ln2 \cdot (X_{ik}))) \qquad (8)$

$$X_{i,k} = \frac{2\theta_i - 2\theta_k}{H_{kj}} \qquad (9)$$

With includes the Caglioti function: $\quad H_{k,Gaussian} = \sqrt{GW + GV \cdot tan\theta + GUtan\theta^2} \qquad (10)$

μ is a mixing parameter, which defines the contribution of the Lorentzian and Gaussian part to the total profile function. The actual value of μ depends on the shape of the observed peaks. The values of μ range from 0 to 1.

Figure 21 shows a Gaussian and a Lorentzian distribution function calculated for a constant integral below the peaks. As can be seen, when the tail of the peak is larger, the Lorentzian function has a higher contribution to the overall peak shape and the mixing parameter μ is larger.
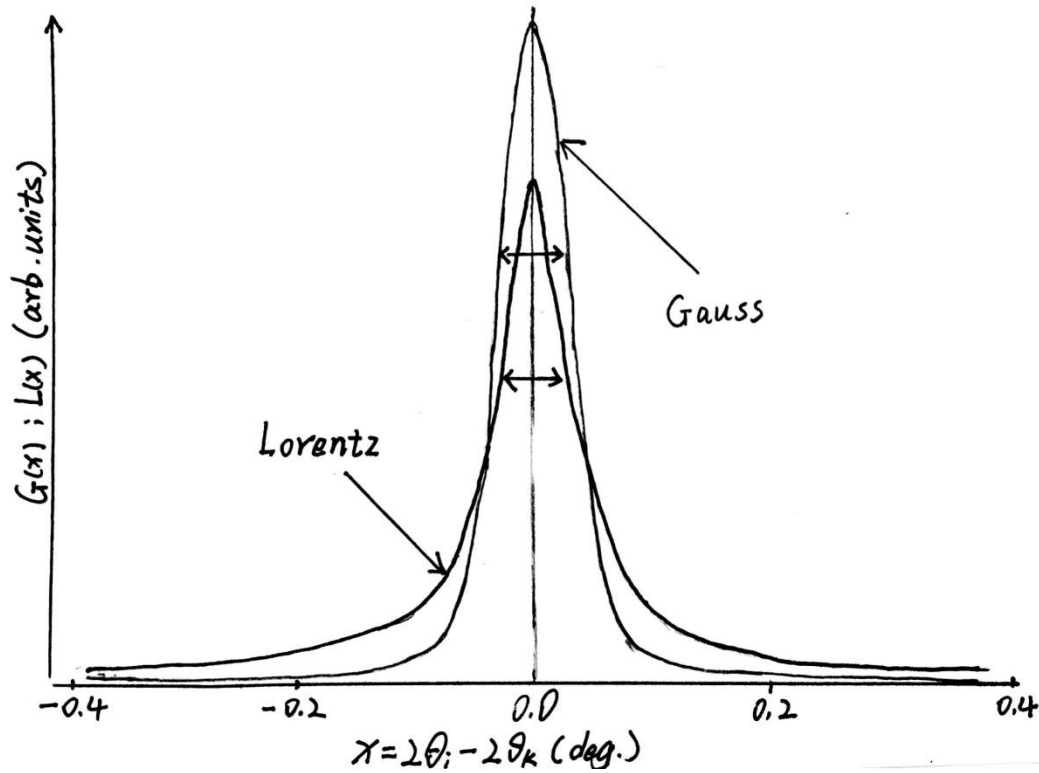
Figure 21: Comparison of a Lorentzian and Gaussian peak shape

The half width of the Lorentzian part is given by equation (6). The parameters LX and LY are parameters which are refined during the LeBail refinement. While LY is correlated with the microstrain on the sample, LX is directly proportional to crystallite size (D^{-1} eq. (7)) (Scherrer equation).

The half width of the Gaussian part is defined by equation (10). Here GW, GV and GU are refinable parameters. The parameter GW fits the half width by a constant value. The fit parameters GV and GU are proportional to the diffraction angle.

In the LeBail refinements of the powder diffraction diagram which were collected on the synthesized samples, the parameters LX, GW and GU were refined.

The background b_{ig}, can be fitted by a mathematical function (e.g. linear interpolation; cosine Fourier series) in which case the number of refinement parameter depend on the shape of the background and has to be adjusted. As an alternative approach the background can also be defined manually.

The zero shift describes an instrumental error (detector zero point error) which results in shifts of the peak positions (also 2θ) and in wrong lattice parameters, if not properly taken into account. The zero shift is usually a parameter which is fitted at an early stage of the Le Bail refinement.

In order to evaluate the results of a Le Bail refinement, standard agreement factors like R_p , R_{wp} and GOF: χ^2 are used. The R_{wp} and R_p values are given by equations (11) and (12).

Weighted profile R-factor: $R_{wp} = \sqrt{\frac{\sum wi(y_{obs}-y_{calc})^2}{\sum_i y^2{}_{obs}}}\%$ (11)

Profile R-factor: $R_p = \frac{y_{calc}-y_{obs}}{y_{calc}}\%$ (12)

In an ideal case, the intensity of both observed and calculated are equal and hence the R-factors will be zero. Accordingly, a higher quality of refinement corresponds to smaller R-factors.

The reduced χ^2 eq. (13) or "goodness of fit" is defined by the minimization function (eq.13) as:

$$GOF: \chi^2 = \frac{\sum wi(y_{obs}-y_{calc})^2}{N_{obs}-N_{parameter}}$$ (13)

Where N_{obs} is the total number of observations in the whole diagram and $N_{parameter}$ is the number of variables in the least squares refinement. When $GOF < 1$ then redundant parameters were simultaneously refined or statistical errors are overweight.

3.4 Refinements of the powder diffraction data

The Le Bail refinements were performed using the program Jana 2006 [20] Initial lattice parameters are from literature (from Chapter: Introduction).

a)

Step	background	shift	Lattice parameter (a,b,c)	Gw	Gu	Lx	100 cycles	Bera's correction
1	x							
2	x	x						
3	x	x					x	
4	x	x	x				x	
5	x	x	x	x			x	
6	x	x	x	x		x	x	
7	x	x	x	x	x	x	x	x

b)

Step	background	shift	Lattice parameter (a,b,c)	Gw	Gu	Lx	100 cycles	Bera's correction
1	x							
2	x	-30						
3	x			x			x	
4	x		x	x			x	
5	x		x	x		x	x	
6	x		x	x	x	x	x	
7	x	x	x	x	x	x	x	x

Table 6: Refinement strategy a) space group R-3m ; b)space group pnma

Le Bail refinements on the compounds Sb_2Te_3; $Sb_2Se_{0.6}Te_{2.4}$; $Sb_2Se_{1.2}Te_{1.8}$; $Sb_2Se_{2.4}Te_{0.6}$ were performed using the refinement strategy shown in table 6(a). At the beginning of the Le Bail refinement the background was fitted using a 20 parameter polynomial function. The peak shape was fitted by a Pseudo-Voigt function, in which the fit parameter (LX)($GW;GU$) were included. In order to improve the errors of the fit parameters, a Berar's correction [14] was applied. The same refinement strategy was applied to all powder data measurement between 20-300 K.

Le Bail refinements on the compounds Sb_2Se_3 were performed using the refinement strategy shown in table 6(b). A refinement of the zero shift at an earlier point of the Le Bail refinement resulted in dubious shifts of the peak postions and hence in wrong lattice parameters. Therefore, the value of the zero shift was fixed at the beginning of the refinement and refined at the end of the refinement. However, the applied refinement strategy is similar to the one shown in table 6(a).

4.Result

4.1 Chemical analysis

The results of the chemical analysis on the samples $Sb_2Se_{0.6}Te_{2.4}(B\&C)$; $Sb_2Se_{1.2}Te_{1.8}(B\&C)$ and $Sb_2Se_{1.8}Te_{1.2}$ are summarized in Table 7, 8, 9. From the determined element concentrations the sum formulas of the synthesized samples were deduced.

$Sb_2Se_{1.8}Te_{1.2}$	Sb / %	Se / %	Te / %
1	47.64	24.82	27.53
2	47.56	24.26	28.18
3	47.60	24.32	28.08
average	47.60	24.17	27.93
theory	45.2	26.4	28.4

Table 7： Chemical analysis of the synthesized sample $Sb_2Se_{1.8}Te_{1.2}$

	Sb / %	Se / %	Te / %
$Sb_2Se_{0.6}Te_{2.4}$-B	41.55	5.78	52.67
$Sb_2Se_{0.6}Te_{2.4}$-C	41.66	5.78	52.59
average	41.61	5.78	52.63
theory	40.8	7.9	51.3
$Sb_2Se_{1.2}Te_{1.8}$-B	44.83	13.46	41.71
$Sb_2Se_{1.2}Te_{1.8}$-C	44.38	13.18	42.43
average	44.61	13.32	42.07
theory	42.9	16.7	40.4

Table 8： Chemical analysis of synthesized samples $Sb_2Se_{0.6}Te_{2.4}$(B&C) and $Sb_2Se_{1.2}Te_{1.8}$(B&C)

	Sb	Se	Te	Summary	ΔSe
$Sb_2Se_{1.8}Te_{1.2}$	2.107	1.669	1.179	$Sb_2Se_{1.584}Te_{1.119}$	0.216
$Sb_2Se_{0.6}Te_{2.4}$-B	2.038	0.437	2.464	$Sb_2Se_{0.429}Te_{2.415}$	0.171
$Sb_2Se_{0.6}Te_{2.4}$-C	2.044	0.434	2.461	$Sb_2Se_{0.425}Te_{2.408}$	0.175
$Sb_2Se_{1.2}Te_{1.8}$-B	2.092	0.968	1.857	$Sb_2Se_{0.925}Te_{1.775}$	0.28
$Sb_2Se_{1.2}Te_{1.8}$-C	2.071	0.948	1.889	$Sb_2Se_{0.915}Te_{1.824}$	0.29

Table 9： Summarized results of the chemical analysis for all synthesized samples

The compounds Sb_2Te_3 and Sb_2Se_3 are close to the expected compositions. A significant deficiency of Se with respect to the originally weighed in amounts was determined for all other samples(See Table 9). Chemical analysis confirms that there exists no significant impurity of further elements in all synthesized samples.

4.2 Sample characterization

4.2.1 Trigonal Sb$_2$Se$_{3-x}$Te$_x$ mixed crystals

Variant A (synthesized in Al$_2$O$_3$ crucible; see also experimental part)

Figure 22 shows the room temperature powder diffractograms measured on the compounds $Sb_2Se_{0.6}Te_{2.4}$; $Sb_2Se_{1.2}Te_{1.8}$;$Sb_2Se_{1.8}Te_{1.2}$; Sb_2Te_3. The measured powder data are compared to diffractogram provided in reference A.N.Mansour [2] on Sb_2Te_3.
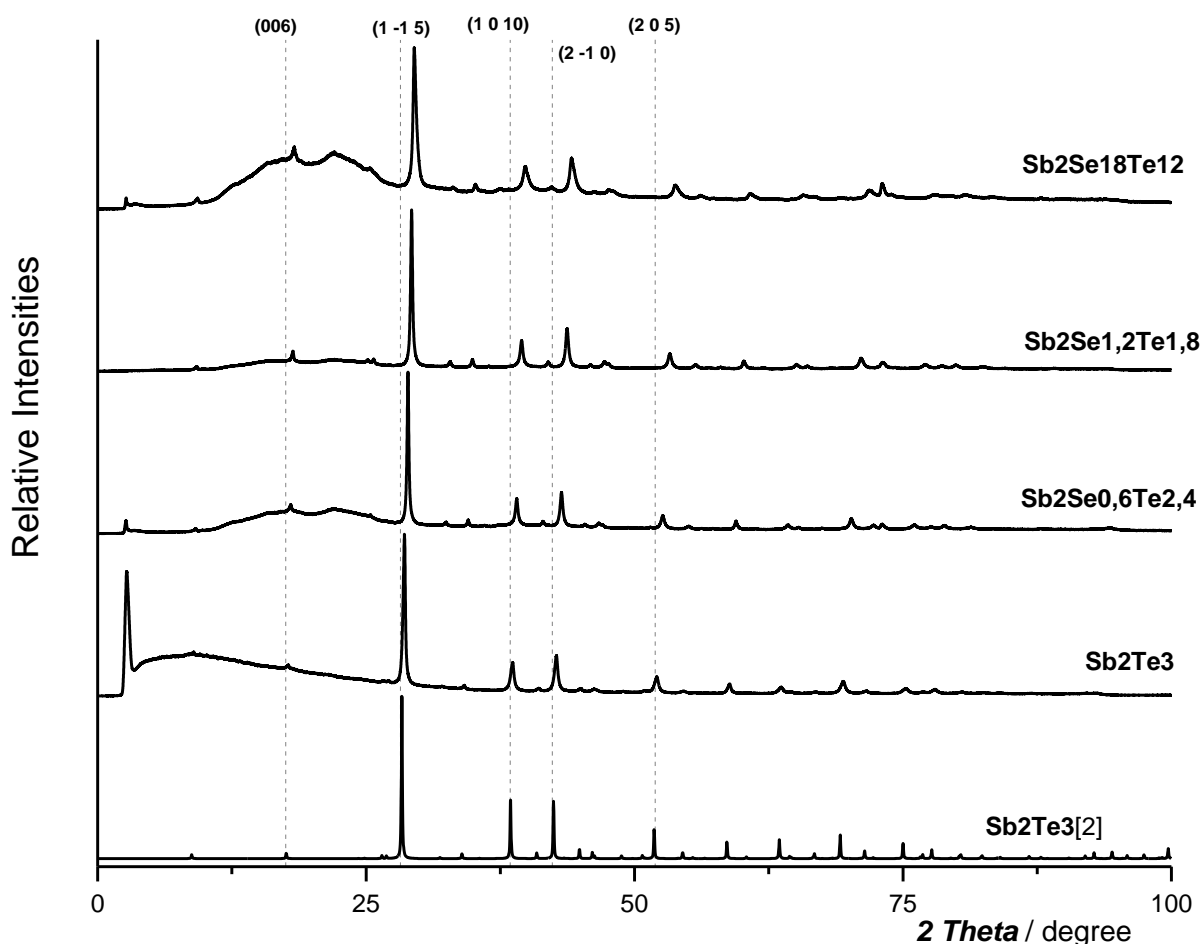
Figure 22: Powder data measured on the products of variant A(see experimental part). The determined data are compared to the diffractogramm of Sb$_2$Te$_3$ published by A.N.Mansour [2].

All detected peaks of all the products can be indexed on the basis of Sb_2Te_3 and no impurities e. g. of the starting materials were found. Therefore, the synthesized products are single phases and are isostructural to Sb_2Te_3. Figure 22 the positions of some representative peaks (e. g. (0 0 6)) of the

products are compared to the ones of Sb_2Te_3 using "auxiliary" lines. This way it becomes evident that the peaks of the synthesized samples shift with increasing *Se* contents to higher 2 Theta angles and hence to smaller lattice parameters (Table 10).

Compounds (300 K)	*a*/ Å	*c*/ Å	*V*/ Å^3	*c/a*	*LX*
Sb_2Te_3	4.2477	30.169	473.88	7.140	17.631
	±0.0012	±0.016	±0.18	-	±1.366
$Sb_2Se_{0.6}Te_{2.4}$	4.2180	30.163	464.85	7.152	15.781
	±0.0007	±0.009	±0.32	-	±1.317
$Sb_2Se_{1.2}Te_{1.8}$	4.1696	29.847	449.37	7.146	18.560
	±0.0004	±0.011	±0.09	-	±0.390
$Sb_2Se_{1.8}Te_{1.2}$	4.1267	29.616	436.78	7.177	22.054
	±0.0027	±0.036	±0.73	-	±2.866

Table 10： Room temperature lattice parameters of the products of variant A and the Lorentzian isotropic crystallite size broadening parameter *LX* as determined by Le Bail refinements

Figure 23 shows the lattice parameters summarized in Table 10 are shown in dependence of the *Se* content. Solid lines represent the case of an ideal miscibility, which is also known as *Vegard's law*. One can see unambiguously that the $Sb_2Se_{3-x}Te_x$ solid solution shows non-ideal miscibility in the stability field of the trigonal phase.
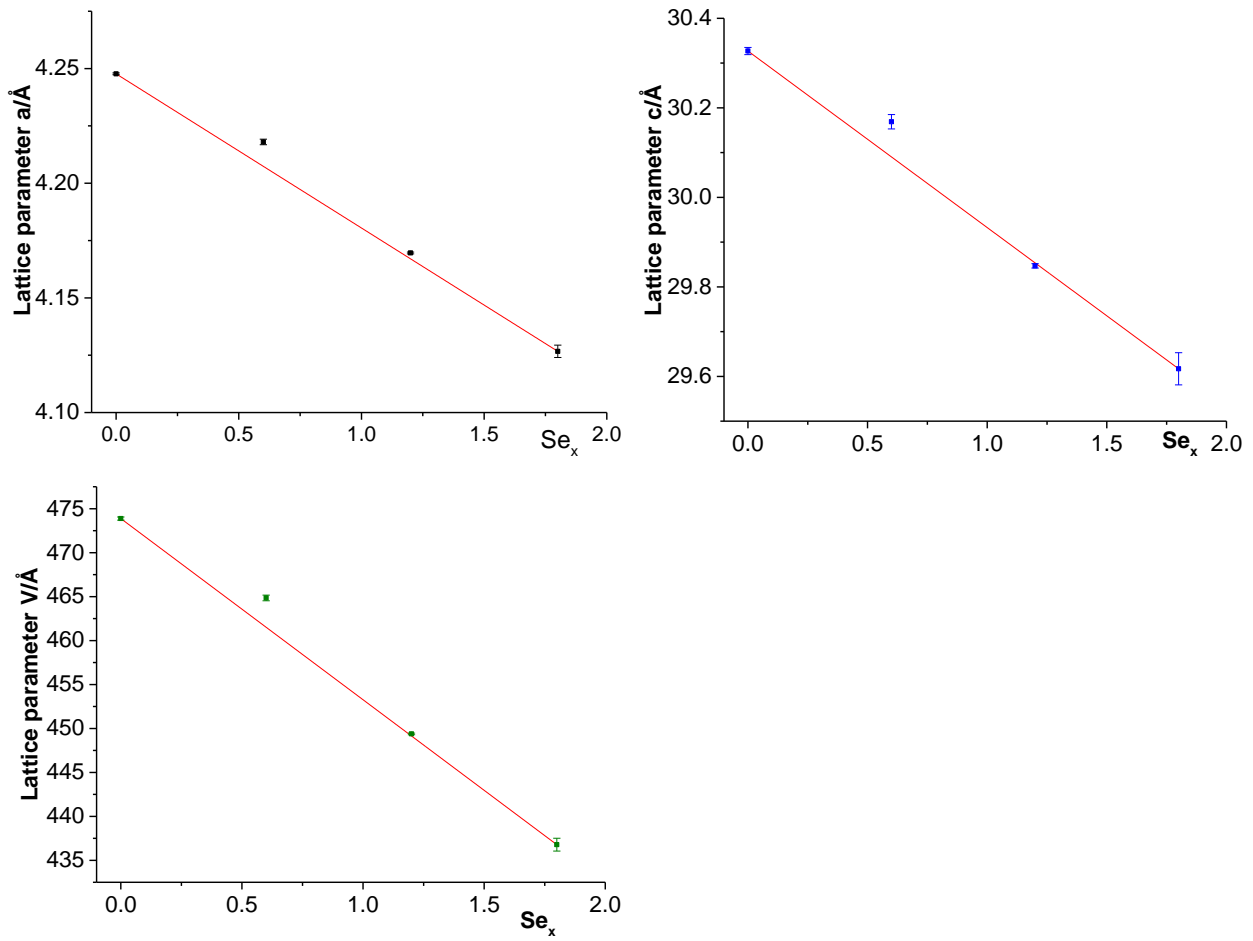
Figure 23: The room temperature lattice parameters of the products of variant A in dependence of the Se content. The The $Sb_2Se_{3-x}Te_x$ solid solutions shows a non-ideal miscibility

Variant *B* (synthesized in Quartz glass crucible) & ***Variant C*** (synthesized in quartz glass crucible covered with B_2O_3; see also experimental part)
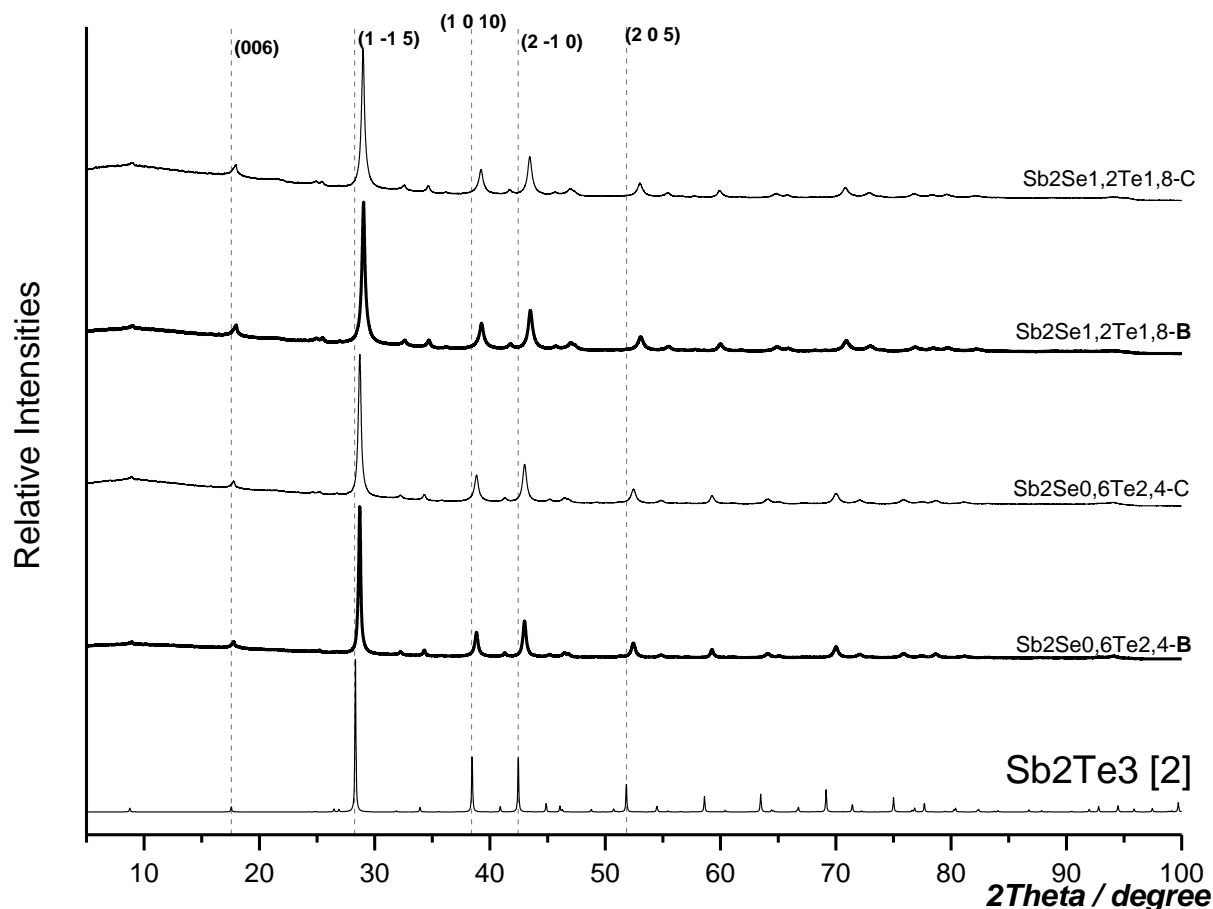
Figure 24: Powder data measured on the products of variant B and C. The measured powder data are compared to the diffractogramm of Sb_2Se_3 determined by A.N.Mansour [2].

Figure 24 shows a comparison between the room temperature powder data measured on the products of variant B and C with the diffractogram provided in reference A.N.Mansour [2] on Sb_2Te_3. All detected peaks of the synthesized products can be indexed on the basis of the structure of Sb_2Te_3 and hence the synthesized products are single phases and are isostructural to Sb_2Te_3.

As can be seen in Figure 24 the powder diffractograms measured on the products of variant *C* show higher background contributions compared to the ones of variant B. This can possibly be attributed to an additional contribution of amorphous B_2O_3 to the background.

In Table 11 the lattice parameters of the products of variant *B* and *C* are summarized. The lattice parameters of the compounds with comparable Se contents synthesized via the two different routes are very similar.

| Compounds (300 K)	a/ Å	c/ Å	V/ Å^3	LX
$Sb_2Se_{0.6}Te_{2.4}$ -B	4.2155	30.1546	464.0724	16.494
	±0.0006	±0.0080	±0.1632	±0.821
$Sb_2Se_{0.6}Te_{2.4}$ -C	4.2151	30.1630	464.1160	17.565
	±0.0007	±0.0090	±0.1851	±1.072
$Sb_2Se_{1.2}Te_{1.8}$- B	4.1698	29.8430	449.3773	30.220
	±0.0010	±0.0114	±0.2355	±1.171
$Sb_2Se_{1.2}Te_{1.8}$ -C	4.1731	29.8661	450.4373	28.213
	±0.0011	±0.0127	±0.2630	±1.365

Table 11： The room temperature lattice parameters of the products of variant B and C and the Lorentzian isotropic crystallite size broadening parameter LX as determined by Le Bail refinements

4.2.2 Crystallite size estimations of trigonal mixed crystals

Table 12 and 13 shows the crystallite size calculated for the products of variant A, B and C using equation ($LX = \frac{1800 \cdot K \cdot \lambda}{D \cdot \pi}$; with LX=Lorentzian isotropic crystallite size broadening parameter, λ=x-ray wavelength, K=dimensionless shape factor with value of 1; D=Crystallite size).

Compounds	Sb_2Te_3	$Sb_2Se_{0.6}Te_{2.4}$	$Sb_2Se_{1.2}Te_{1.8}$	$Sb_2Se_{1.8}Te_{1.2}$
Crystallite size/nm	50.047	55.912	47.540	40.010
Error/nm	±7.749	±8.347	±2.102	±12.999

Table 12： The crystallite sizes of the products of variant A

Compounds	$Sb_2Se_{0.6}Te_{2.4}$		$Sb_2Se_{1.2}Te_{1.8}$	
	B	C	B	C
Crystallite size/nm	53.496	50.234	29.198	31.275
Error/nm	±2.663	±3.066	±1.131	±1.513

Table 13： The crystallite sizes of the products of variant B and C

For sample $Sb_2Se_{0.6}Te_{2.4}$ the determined crystallite sizes of all products are comparable. In case of sample $Sb_2Se_{1.2}Te_{1.8}$ the determined crystallite sizes are the largest for variant A and are comparable for variant B and C.

4.2.3 Orthorhombic Sb₂Se₃ mixed crystals

Figure 25 shows a comparison between the room temperature powder diffractogram of the Sb_2Se_3 sample synthesized in this study with the one measured by [3]. All measured peaks can be indexed on the basis of the structure published in [3] and hence the synthesized sample is a pure phase.
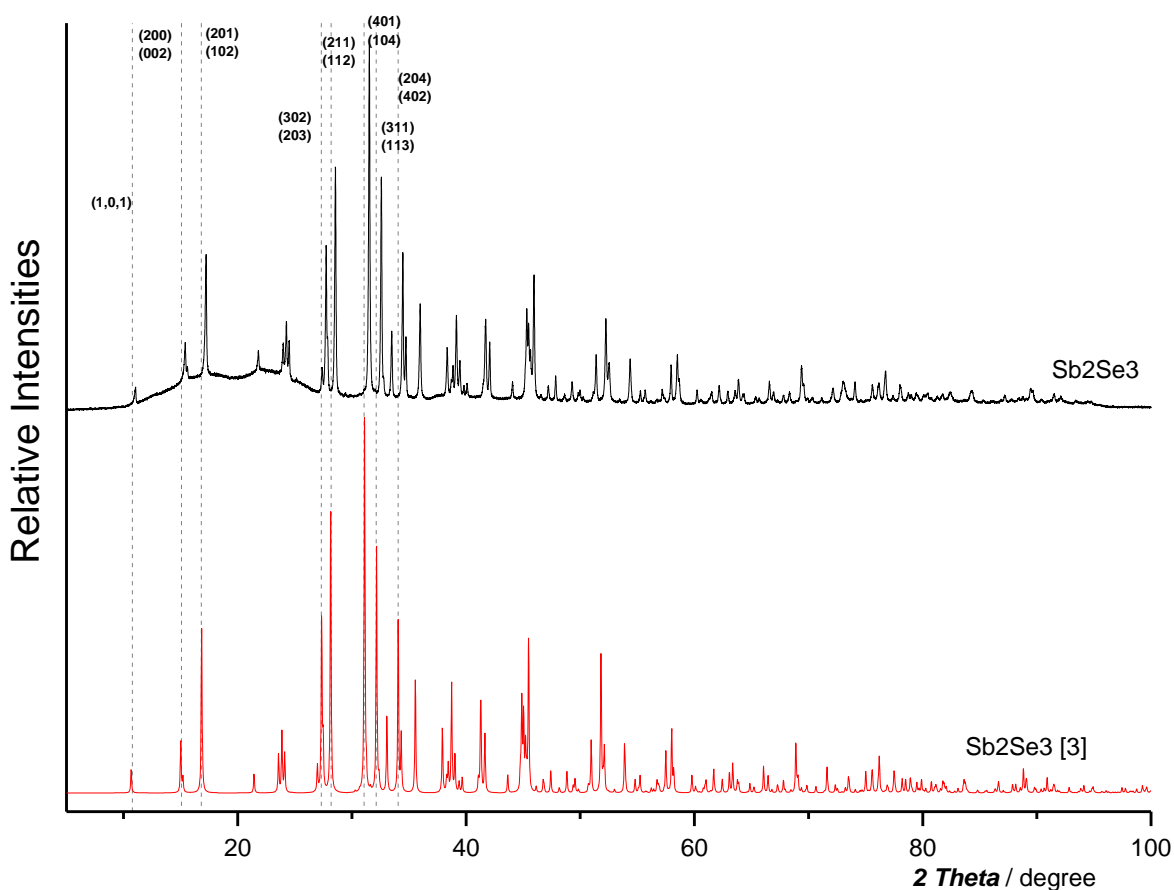
Figure 25: Comparison of powder diffractogram of the synthesized Sb₂Se₃ sample with the one measured by Voutsas, et al. [3].

The lattice parameters determined in this study are different to the published one Voutsas, et al. [3] based on single crystal diffraction measurements (Table 16). We assume that the differences could be due to an absolute offset between the powder and single crystal diffractometer. Also, the chemical composition of the sample in the literature is not mentioned.

Compounds(300k)	a/Å	b/Å	c/Å	V/Å^3	LX
Sb_2Se_3	11.7752	3.9749	11.6255	544.1298	7.009
	±0.0006	±0.0018	±0.0005	±0.0562	±0.275
Sb_2Se_3	11.7938	3.9858	11.6478	547.536	
[3]	±0.0009	±0.0006	±0.0007	±0.0378	

Table 14: Comparison of the room temperature lattice parameters of the synthesized Sb_2Se_3 sample and the ones published in the literature by Voutsas, et al.[3]

4.2.4 Crystallite size estimation of Orthorhombic mixed crystals

For the Sb_2Se_3 sample a crystallite size of 126(4) nm was calculated using eq. $LX = \frac{1800 \cdot K \cdot \lambda}{D \cdot \pi}$ (see chapter 4.2.2). The crystallite size of the Sb_2Se_3 sample is obviously larger than the one of the trigonal $Sb_2Se_{3-x}Te_x$ mixed crystals.

4.3 Temperature dependence of relative lattice parameters

4.3.1 Trigonal Sb₂Se₃₋ₓTeₓ mixed crystals

Figures 26-28 show the temperature dependence of the relative lattice parameters of the samples $Sb_2Se_{0.6}Te_{2.4}$; $Sb_2Se_{1.2}Te_{1.8}$; $Sb_2Se_{1.8}Te_{1.2}$ and Sb_2Te_3 between 20-300 K. All three lattice parameters and unit cell volumes show small variations as a function of temperature. For all samples the relative lattice parameters decrease down to 50 K. At this temperature a minimum is reached. The temperature dependent changes of the relative lattice parameter a increase with increasing Se contents in the samples. On the other hand, the c-lattice parameter of the samples Sb_2Te_3 , $Sb_2Se_{0.6}Te_{2.4}$ and $Sb_2Se_{1.2}Te_{1.8}$ show very similar temperature dependences and only for the sample with the highest Se-content $(Sb_2Se_{1.8}Te_{1.2})$ the lattice parameter exhibits a significantly stronger change as a function of

temperature. Furthermore, the temperature dependences of the lattice parameters of all compounds show anomalies at different temperatures. For all these anomalies the powder diffraction diagrams above and below the relevant temperature were carefully compared. As an example, Figure 31-33 show some representative diffractograms of $Sb_2Se_{0.6}Te_{2.4}$ $Sb_2Se_{1.2}Te_{1.8}$ and $Sb_2Se_{1.8}Te_{1.2}$ measured above and below the observed anomalies. As can be seen, no drastic changes in the powder diffraction diagrams were detected. Thus, the observed anomalies are most likely not caused by structural phase transitions, but can rather be attributed to small changes in the thermal expansion of the respective compounds. Similar results were obtained by A. N. Mansour [2], X. Chen [4] and D. Bessas [1](see Figure 28-30 and the normalized lattice parameter a and c as well as the temperature dependence of normalized c/a ratio are comparable. There exists a small offset between the data obtained from the LeBail refinement in this work and the literature data. This might be due to slightly different chemical compositions of the sample. However, it is not possible to prove this assumption as no chemical analysis is provided in the literature.
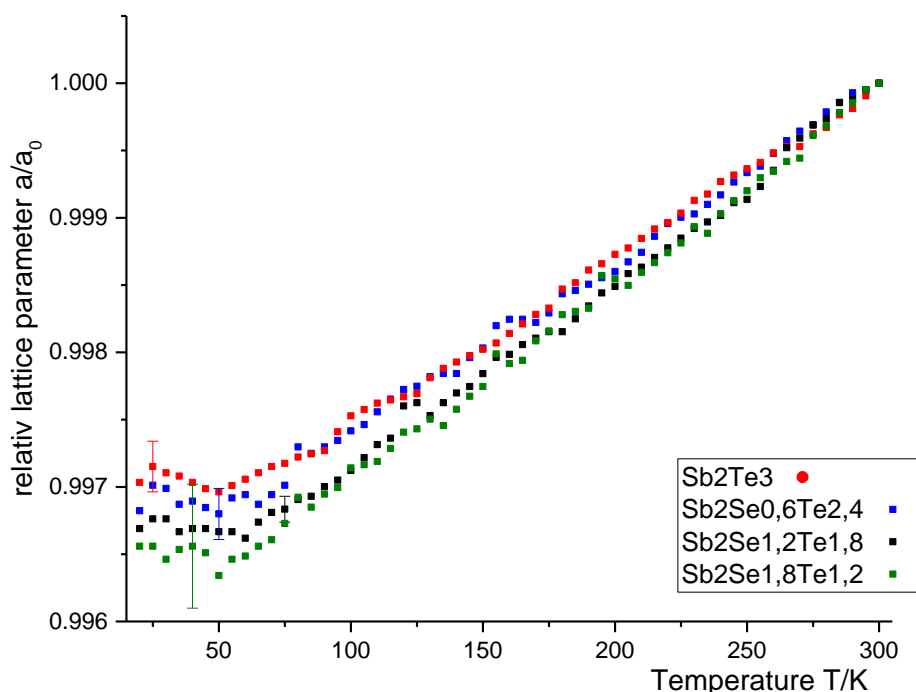
Figure 26: The temperature dependence of the normalized lattice parameter a of the samples Sb_2Te_3; $Sb_2Se_{0.6}Te_{2.4}$; $Sb_2Se_{1.2}Te_{1.8}$; $Sb_2Se_{1.8}Te_{1.2}$
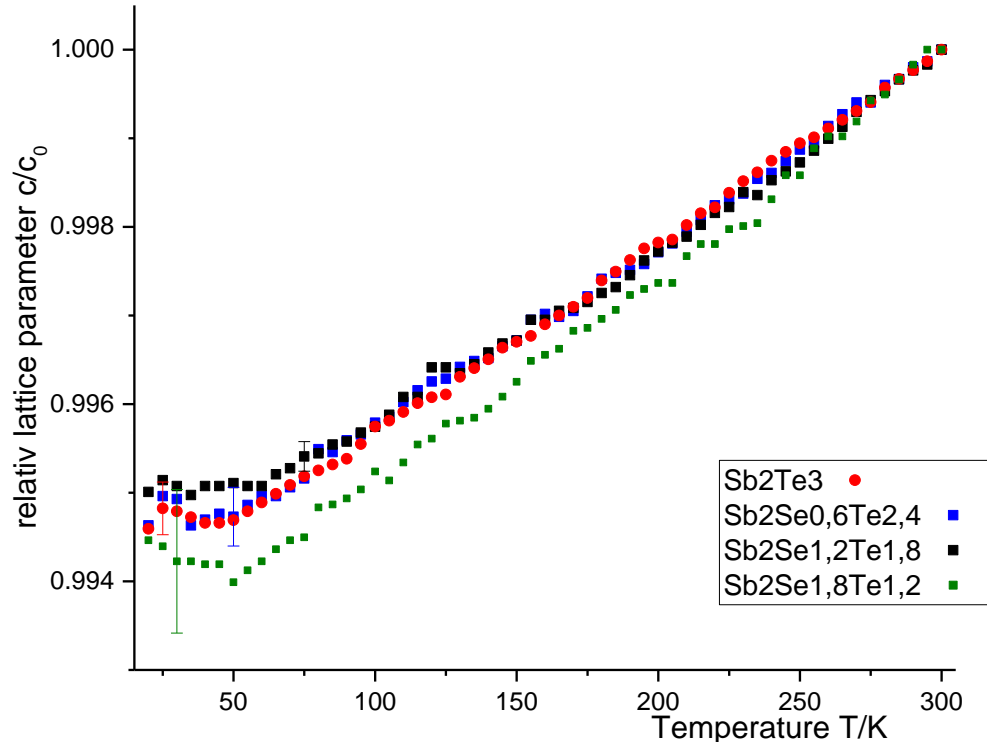
Figure 27: The temperature dependence of the normalized lattice parameter *a* of the samples Sb$_2$Te$_3$; Sb$_2$Se$_{0.6}$Te$_{2.4}$; Sb$_2$Se$_{1.2}$Te$_{1.8}$; Sb$_2$Se$_{1.8}$Te$_{1.2}$
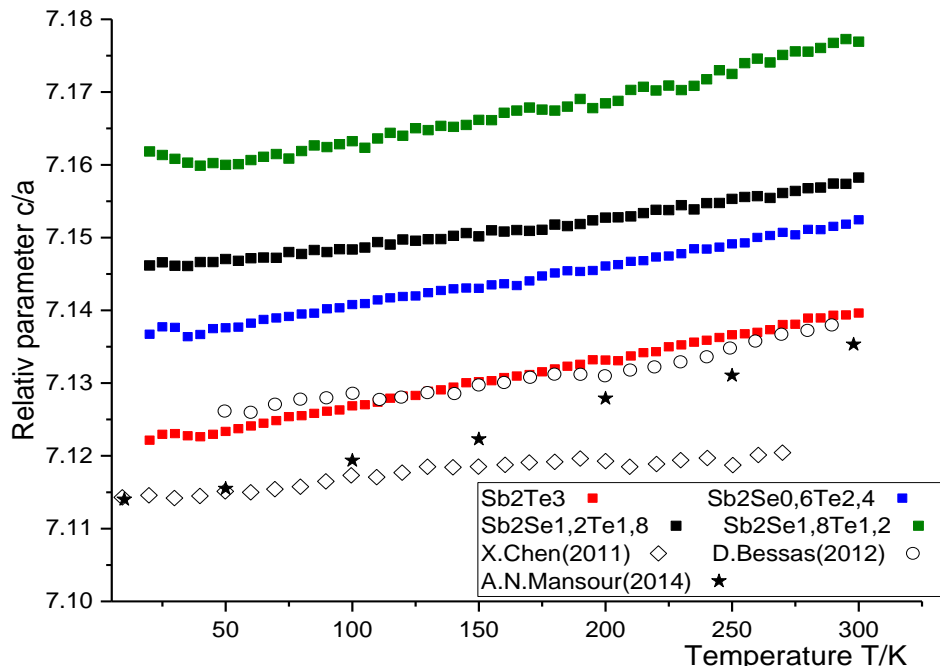
Figure 28: The temperature dependence of the normalized *c/a* ratio of the samples Sb$_2$Te$_3$; Sb$_2$Se$_{0.6}$Te$_{2.4}$; Sb$_2$Se$_{1.2}$Te$_{1.8}$; Sb$_2$Se$_{1.8}$Te$_{1.2}$ and comparison to the literature data by A.N.Mansour[2], X.Chen[4] and D.Bessas[1]
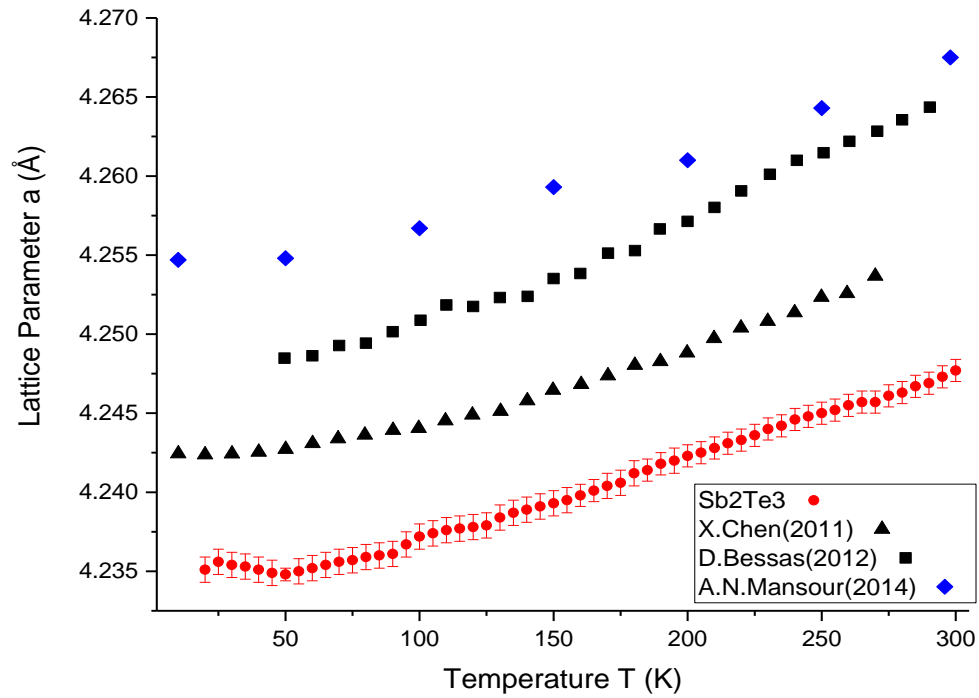
Figure 29: Temperature dependence of the normalized lattice parameter a of Sb$_2$Te$_3$ and comparison to literature data from A.N.Mansour[2], X.Chen[4] and D.Bessas[1]
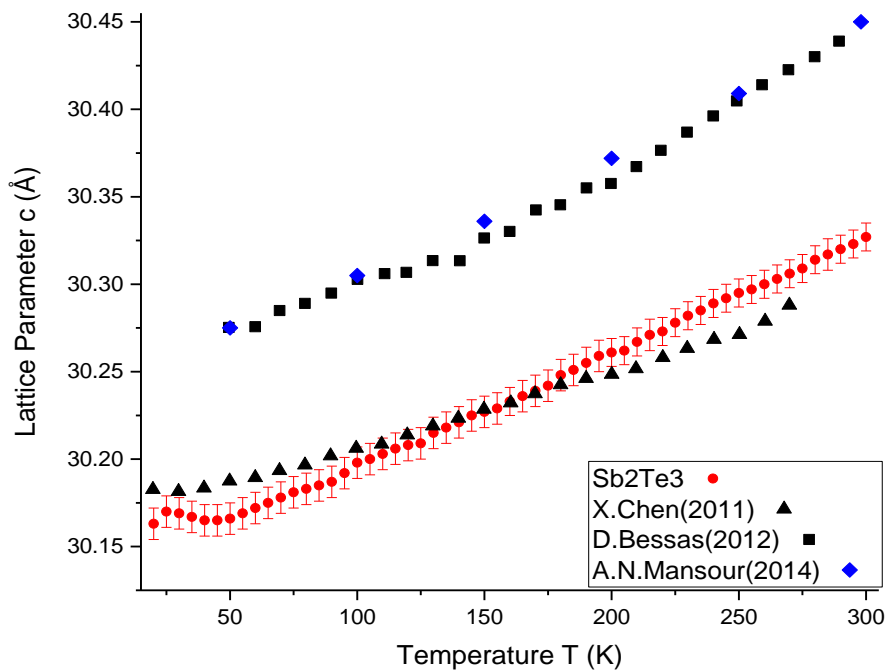
Figure 30: The temperature dependence of the normalized lattice parameter c of Sb$_2$Te$_3$ and comparison to literature data by A.N.Mansour[2], X.Chen[4] and D.Bessas[1]
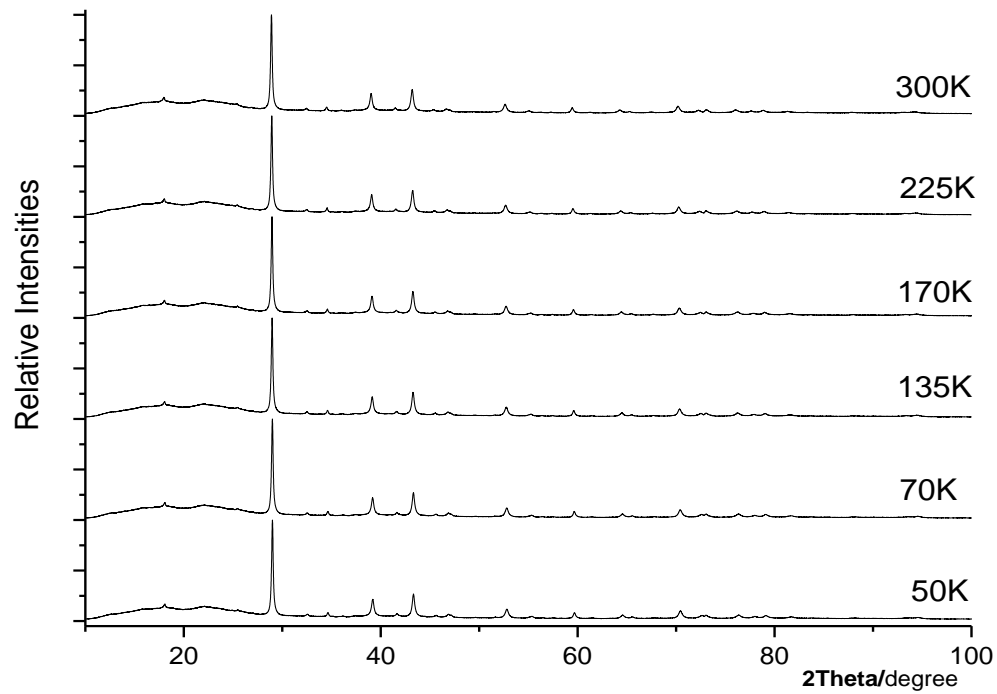
Figure 31: Representative diffractograms measured above and below the anomalies of $Sb_2Se_{0.6}Te_{2.4}$
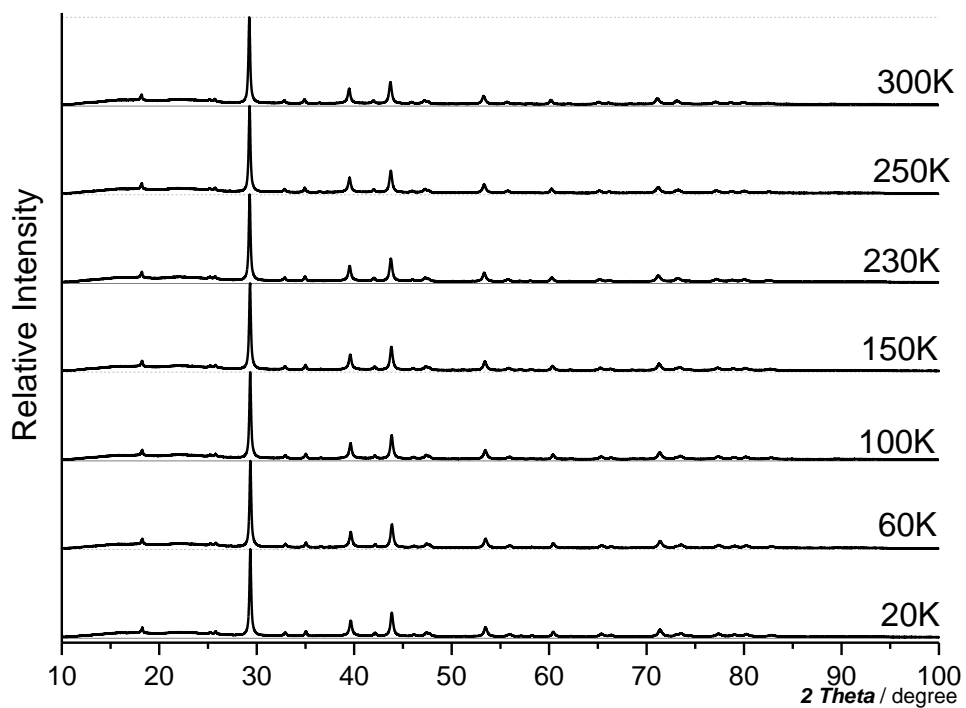
Figure 32: Representative diffractograms measured above and below the anomalies of $Sb_2Se_{1.2}Te_{1.8}$
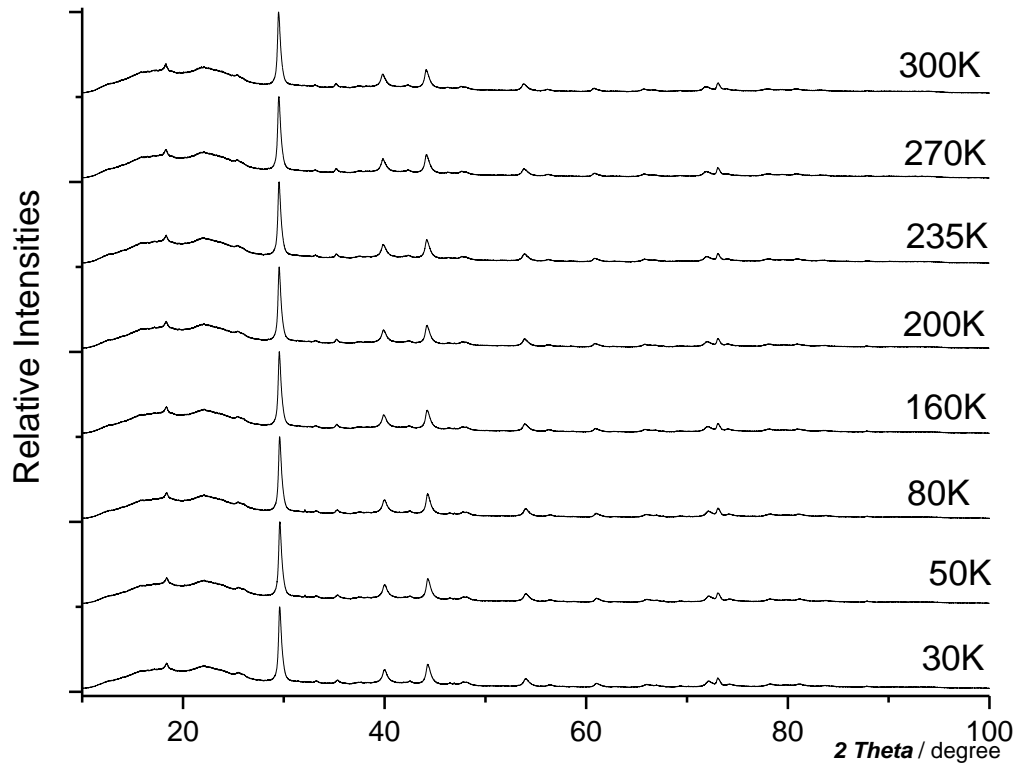
Figure 33: Representative diffractograms measured above and below the anomalies of $Sb_2Se_{1.8}Te_{1.2}$

4.3.2 Orthorhombic Sb₂Se₃ mixed crystals

Figure 34 shows the temperature dependence of the relative lattice parameters of the samples Sb_2Se_3 between 20 K and 300 K. In Sb_2Se_3 all lattice parameter show a similar temperature dependency. The *c*-lattice parameter shows the largest decrease with decreasing temperature. The relative change of the lattice parameters *b* and *c* is equal in the range about 125 K to 300 K. At lower temperatures the *b*-lattice parameter shows a stronger decrease than the *a*-lattice parameter. For all three lattice parameter a minimum was observed at about 40 K.
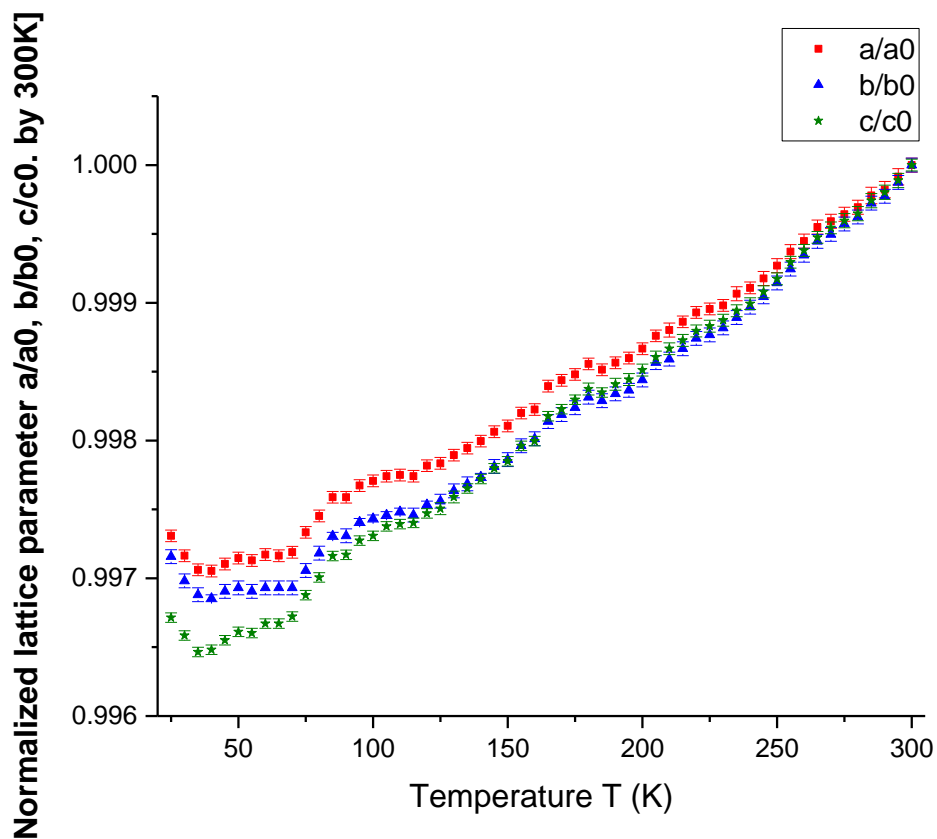
Figure 34: The temperature dependence of the normalized lattice parameter *a, b and c* of the sample Sb_2Se_3

Furthermore, for all lattice parameters some small anomalies were observed around 20 K, 40 K, 60 K, 115 K, 165 K, 200 K, 250 K, and 270 K. Figure 35 shows some representative diffractograms measured above and below the anomalies. As there are no additional peaks appearing and the intensities at the different temperatures are comparable, it is reasonable to assume that the observed anomalies are not caused by any structural phase transitions.
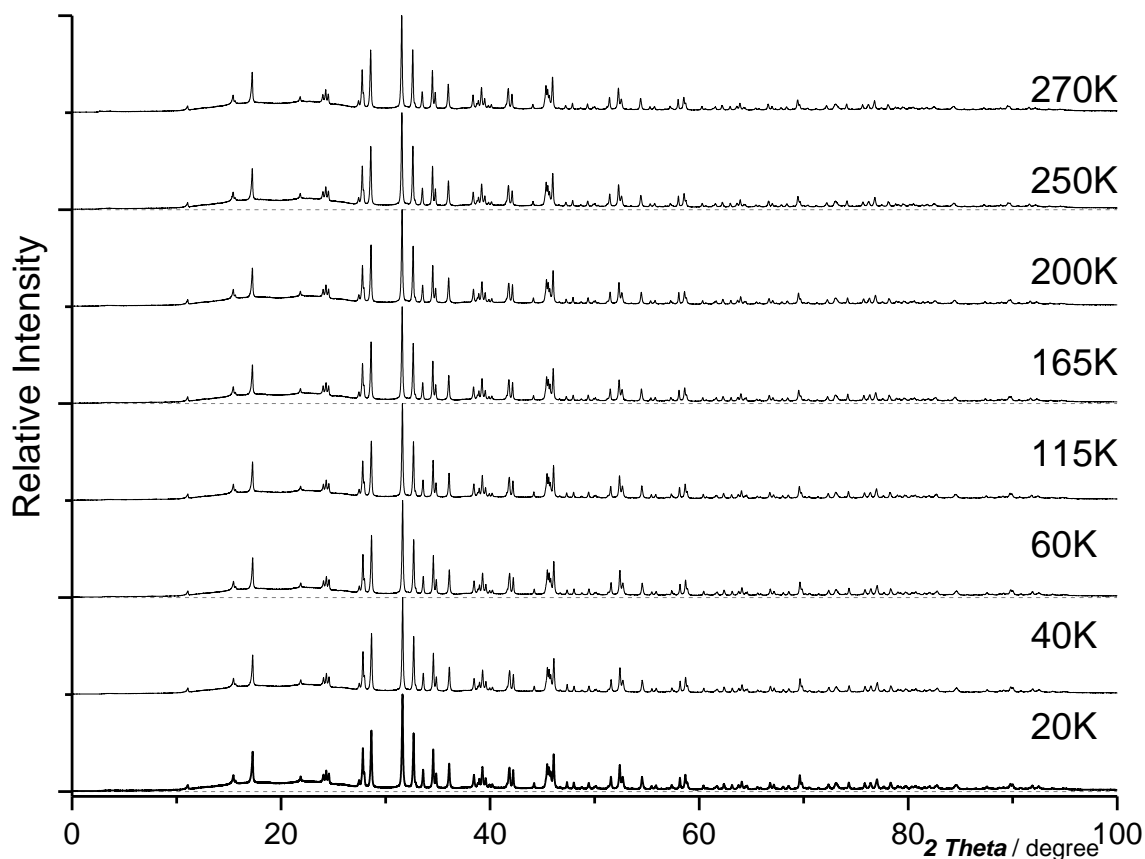
Figure 35: Representative diffractograms measured above and below the anomalies of Sb$_2$Se$_3$

4.3.3 Thermal expansions of Sb$_2$Se$_{3-x}$Te$_x$ mixed crystals

From the variation of the lattice parameter and the unit cell volume as a function of the temperature, one can obtain the thermal expansion of the *a-* and *c-*lattice parameters as well as the thermal expansion of the unit cell volume for the $Sb_2Se_{3-x}Te_x$ mixed crystals. The calculated thermal expansions are shown in Table 15. As one can see from the table, the thermal expansion of the unit cell volume for the $Sb_2Se_{3-x}Te_x$ mixed crystals is increasing with elevated Se contents within the trigonal phase.

Compounds	$1 - \dfrac{a(T=50K)}{a(T=300K)} \cdot 100\%$	$1 - \dfrac{b(T=50K)}{b(T=300K)} \cdot 100\%$	$1 - \dfrac{c(T=50K)}{c(T=300K)} \cdot 100\%$	$1 - \dfrac{V(T=50K)}{V(T=300K)} \cdot 100\%$
Sb_2Te_3[2]	0.295(7)	0.295(7)	0.575(10)	1.160(19)
Sb_2Te_3	0.304(9)	0.304(9)	0.531(29)	1.131(19)
$Sb_2Se_{0.6}Te_{2.4}$	0.320(19)	0.320(19)	0.527(33)	1.162(43)
$Sb_2Se_{1.2}Te_{1.8}$	0.333(10)	0.333(10)	0.489(17)	1.153(22)
$Sb_2Se_{1.8}Te_{1.2}$	0.366(45)	0.366(45)	0.601(80)	1.326(11)
Sb_2Se_3	0.285(4)	0.307(s)	0.339(3)	0.928(9)

Table 15: Thermal expansion of the *a*-, *b*-, *c*-lattice parameter and the unit cell volume V for $Sb_2Se_{3-x}Te_x$

4.4 Statistical evaluation of refinement results

4.4.1 Standard agreement factors of refinement

Table 16 the values of the statistical parameters $GOF: \chi^2$, R_p , R_{wp} of the aforementioned Le Bail refinements on the investigated samples are summarized. Although the obtained mean statistical parameters show that the Le Bail fits were not ideal (the factors $GOF: \chi^2$ of all compounds are over 1 and theoverall agreement factors R_p ; R_{wp} are around 3.0-3.8 % and 4.6-5.4 %), the statistical parameter show that the refinements are sufficiently reliable for an interpretation of the measured data.

	$\overline{\chi^2}$	$\overline{R_p}$ / %	$\overline{R_{wp}}$ / %
Sb_2Te_3	2.6(1)	3.8(2)	5.4(3)
$Sb_2Se_{0.6}Te_{2.4}$	3.2(3)	3.3(1)	5.1(4)
$Sb_2Se_{1.2}Te_{1.8}$	2.1(2)	3.6(4)	4.9(5)
$Sb_2Se_{1.8}Te_{1.2}$	3.3(4)	3.0(3)	4.6(5)
Sb_2Se_3	3.0(2)	3.7(1)	5.3(1)

Table 16: Mean of the statistical parameters R_p, R_{wp} and GOF:χ^2 obtained from the Le Bail refinements on the $Sb_2Se_{3-x}Te_x$ mixed crystals

4.4.2 Analysis of the Zero shift parameter

To ensure the quality of refinement data and compare the anomalies of the diffractogram, Figure 36-40 show a summary of the refined values of the zero shift obtained from the Le Bail refinements of the $Sb_2Se_{0.6}Te_{2.4}$, $Sb_2Se_{1.2}Te_{1.8}$, $Sb_2Se_{1.8}Te_{1.2}$, Sb_2Te_3 and Sb_2Se_3 mixed crystals.

As can be seen, at the lowest temperatures from 20 K to 50 K the values of the zero shift of the compounds $Sb_2Se_{3-x}Te_x$ are significantly larger than the average value.

For the Se-end member Sb_2Se_3 the value of the zero shift parameter shows significant deviations from the average value in the temperature ranges between 25-30 K, 85-105 K and 225-245 K.
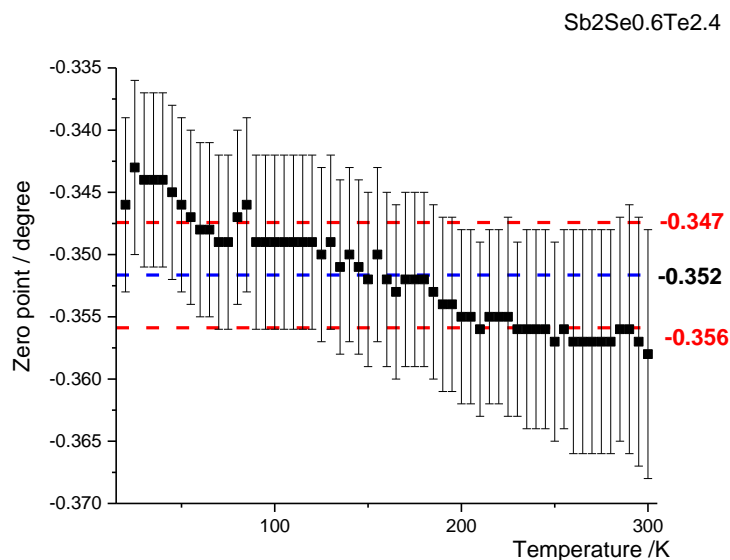
Figure 36: Value of the zero shift parameters at each measured temperature of $Sb_2Se_{0.6}Te_{2.4}$
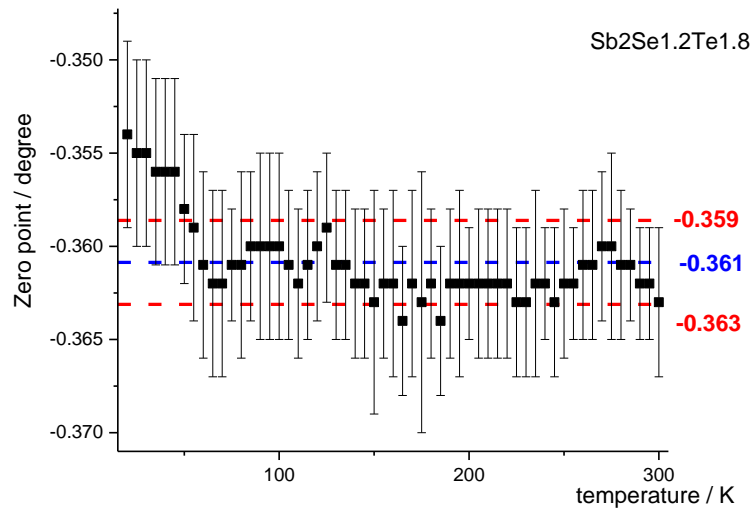
Figure 37: Value of the zero shift parameters at each measured temperature of $Sb_2Se_{1.2}Te_{1.8}$
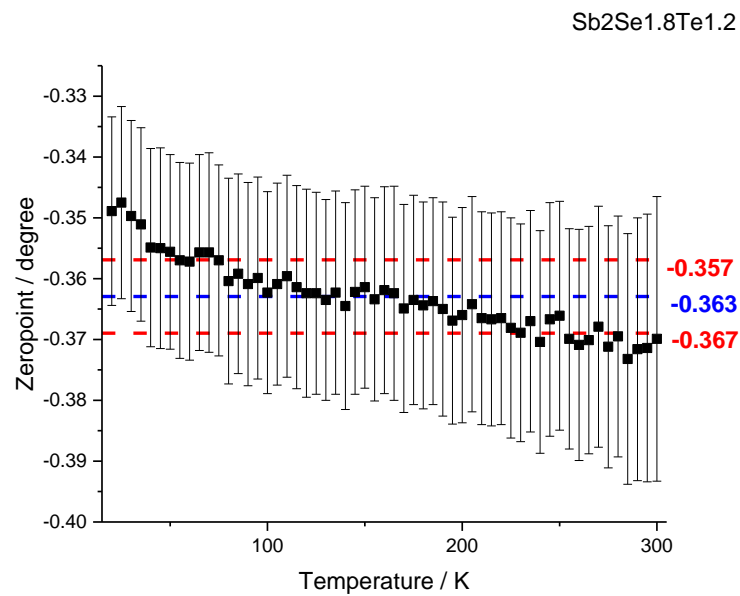
Figure 38: Value of the zero shift parameters at each measured temperature of $Sb_2Se_{1.8}Te_{1.2}$
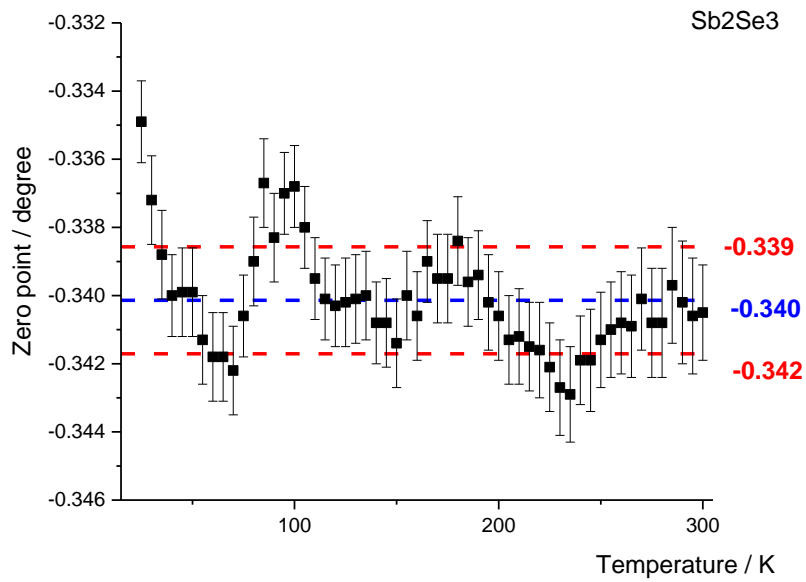
Figure 39: Value of the zero shift parameters at each measured temperature of Sb_2Se_3
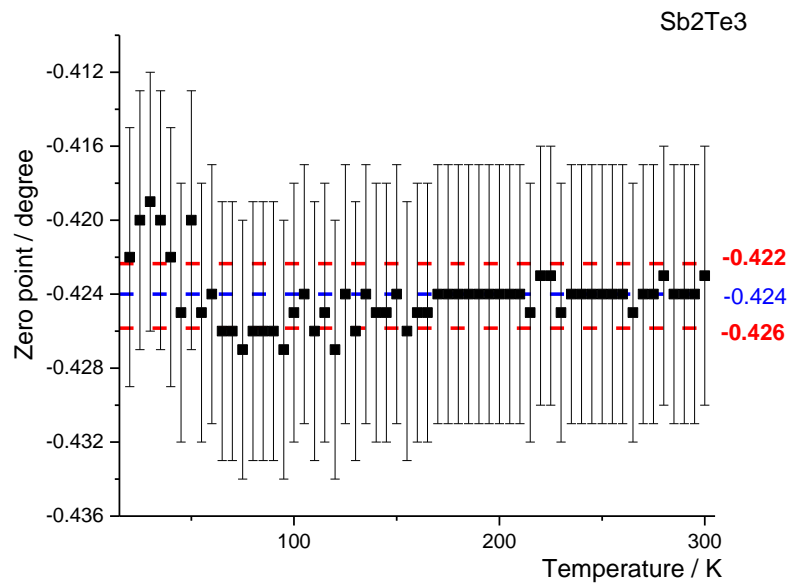
Figure 40: Value of the zero shift parameters at each measured temperature of Sb_2Te_3

4.4.3 Recalculated temperature dependence of relative lattice parameters

As the analysis of the zero shift parameter indicated an anomalous behavior at the lowest temperatures, the normalized lattice parameter of the samples $Sb_2Se_{0.6}Te_{2.4}$; $Sb_2Se_{1.2}Te_{1.8}$ and $Sb_2Se_{1.8}Te_{1.2}$ were recalculated in the temperature range from 20-55 K using the average values of the zero shift parameters(see Figure 41-43). The refinement strategy for the recalculation shown in the attachment [Table B].
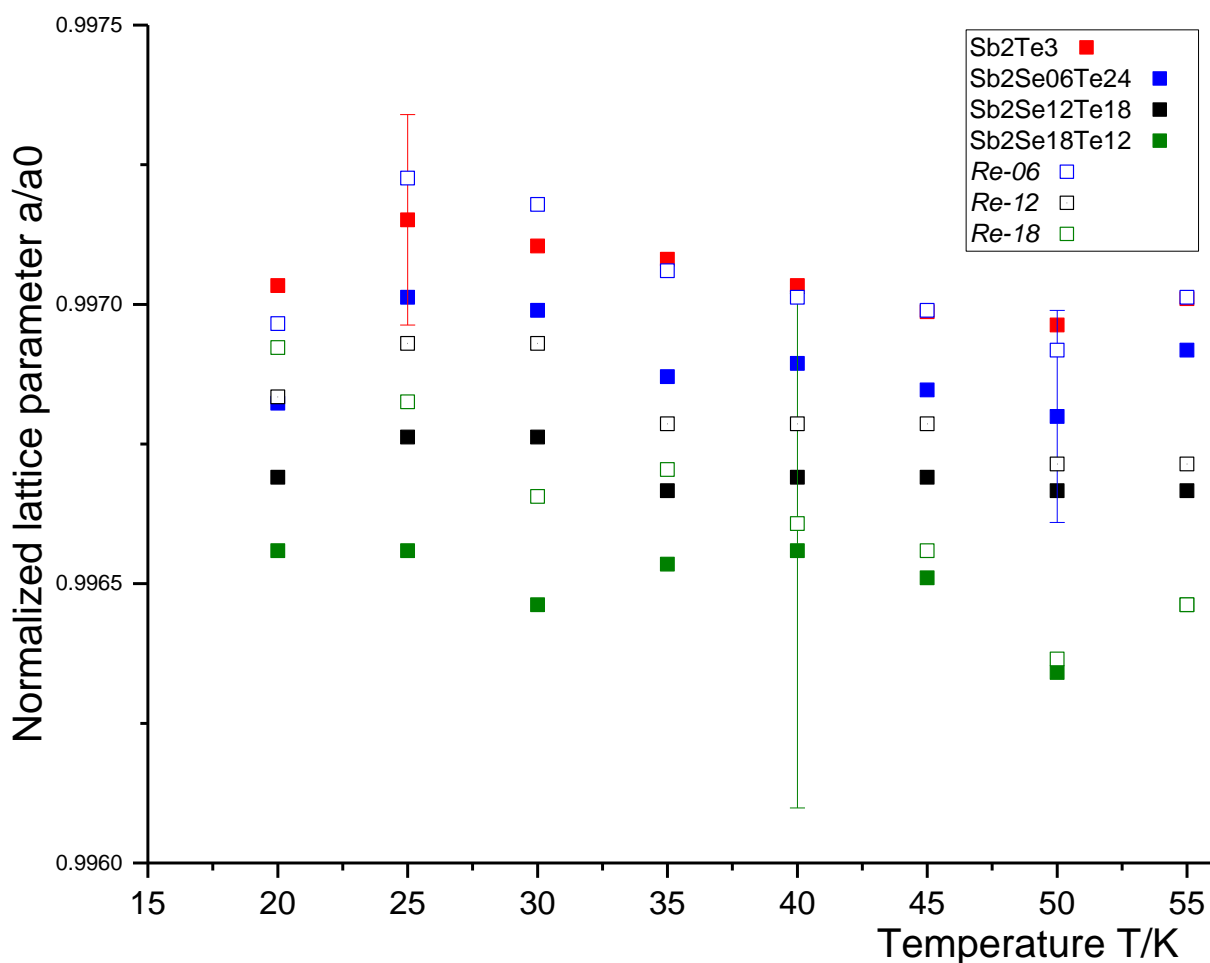
Figure 41: Comparison of the original and recalculated normalized lattice parameter *a/a0* against temperature for Sb_2Te_3; $Sb_2Se_{0.6}Te_{2.4}$; $Sb_2Se_{1.2}Te_{1.8}$; $Sb_2Se_{1.8}Te_{1.2}$ in the temperature range from 20-55 K
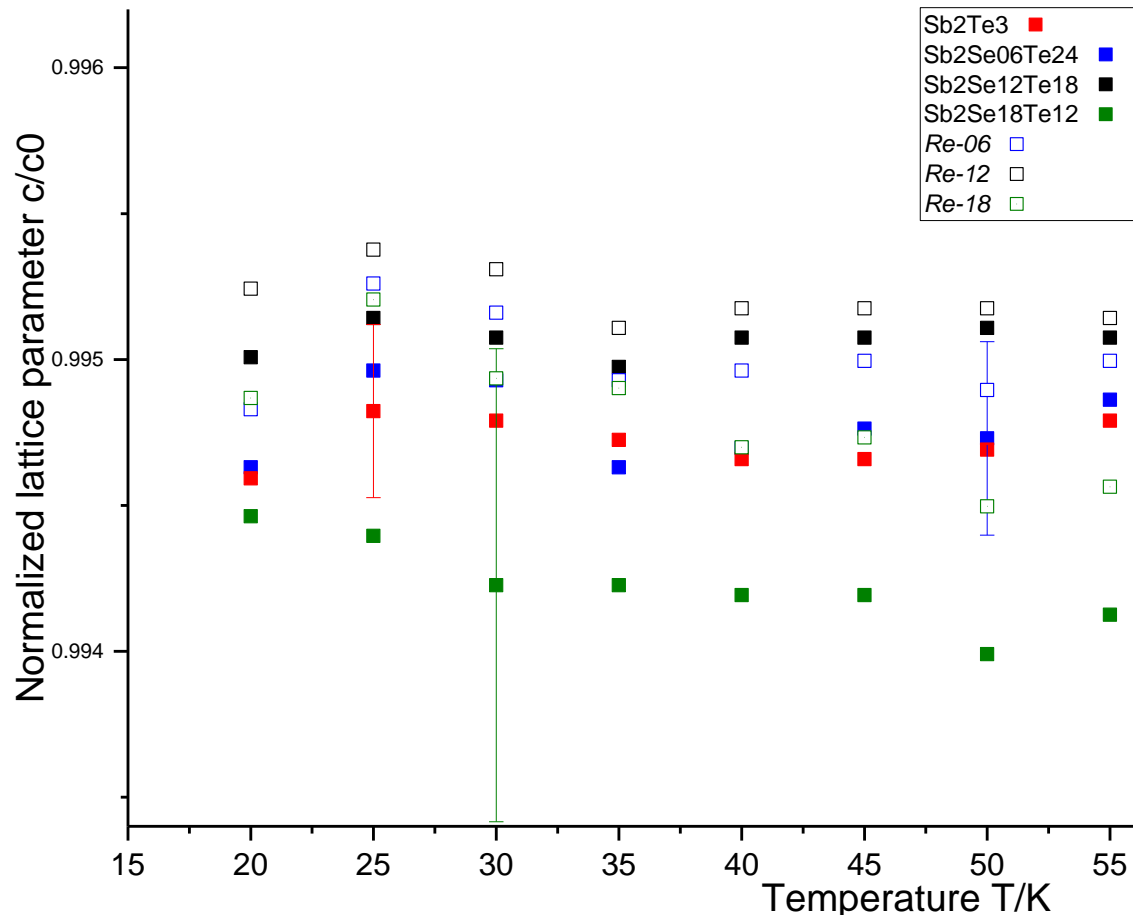
Figure 42: Comparison of the original and recalculated normalized lattice parameter *c/c0* against temperature for Sb$_2$Te$_3$; Sb$_2$Se$_{0.6}$Te$_{2.4}$; Sb$_2$Se$_{1.2}$Te$_{1.8}$; Sb$_2$Se$_{1.8}$Te$_{1.2}$ in the temperature range from 20-55 K

As can be seen from Figure 41 and 42 the recalculated normalized lattice parameters of $Sb_2Se_{0.6}Te_{2.4}$; $Sb_2Se_{1.2}Te_{1.8}$ and $Sb_2Se_{1.8}Te_{1.2}$ lead to a smaller decrease of the lattice parameter with decreasing temperature as the original values. The influence of the zero shift parameter on the *c*-lattice parameter is larger than on the *a*-lattice parameter.
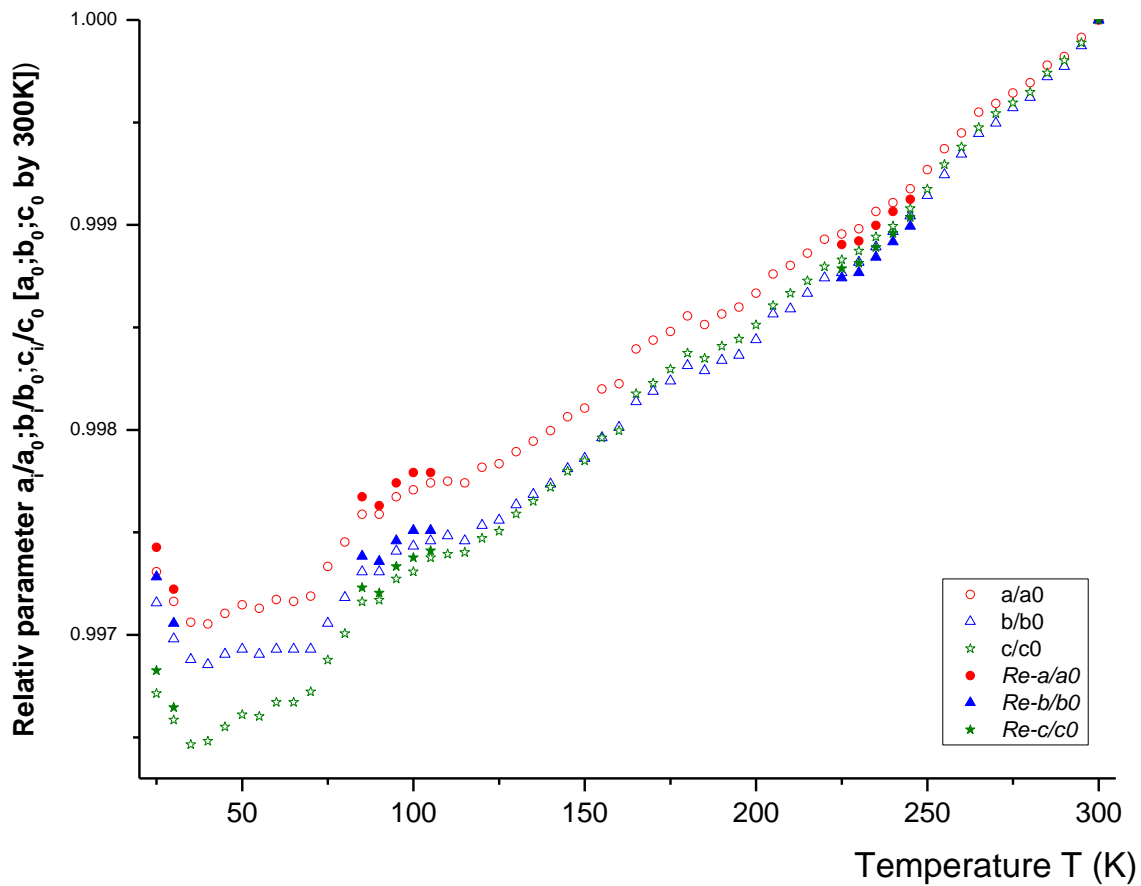
Figure 43: Comparison of original and recalculated normalized lattice parameters of Sb_2Se_3

In Figure 43 the recalculated and normalized lattice parameters of the Sb_2Se_3 end member are depicted in the temperature ranges between 25-30 K; 85-105 K and 225-245 K. For the Sb_2Se_3 sample the temperature dependence of the recalculated and original data are in a good agreement. Moreover, the observed anomalies in the temperature dependence of the normalized lattice parameters are even more pronounced in the case of the recalculated data.

5. Discussion

In this study, the thermal behavior of the lattice parameters of selected $Sb_2Se_xTe_{3-x}$ mixed crystals with representative compositions (x=0, 0.6, 1.2, 1.8, 3) have been studied by X-ray powder diffraction as a function of temperature. The measurements were performed between 20-300 K with steps of 5 K. The small temperature interval was chosen in order to improve the resolution of the temperature dependent anomalies observed in previous studies [1,2,4].

5.1 Discussion of synthesized compounds

Table 4 shows the yields of the compounds synthesized according to the different synthesis routes A, B and C. The yields of Variant B are comparable with the one of Variant A. The yields of variant C are both over 100%. Therefore, the products of the synthesis contain a part of the covering material B_2O_3. It was assumed that the yields of the desired products $Sb_2Se_{0.6}Te_{2.4}$ and $Sb_2Se_{1.2}Te_{1.8}$ of variant C are the same as variant B. By this assumption the amounts of the covering material B_2O_3 in the products of variant C were estimated and are given in Table 17.

Variant C	B_2O_3 / g	Summary / g	Output / g	B_2O_3 remains / g
$Sb_2Se_{0.6}Te_{2.4}$	0.208	2.20829	2.033	0.0347
$Sb_2Se_{1.2}Te_{1.8}$	0.219	2.20677	2.039	0.0532

Table 17: Calculation of the B_2O_3 amount of the samples (variant C)

The results of the chemical analysis have shown a pronounced Se loss for the slowly cooled samples $Sb_2Se_{0.6}Te_{2.4}$ and $Sb_2Se_{1.2}Te_{1.8}$ mixed crystals of variant B and C Table 8 and 9. Gosain et al.[9]have reported the melting points of about 410°C for some $Sb_2Se_xTe_{3-x}$ mixed crystals in the stability field of the Sb_2Te_3 crystal structure. Therefore, the Se loss most probably occurs during the cooling process from the reaction temperature to the crystallization point.

5.2 The thermal behavior of lattice parameters

5.2.1 Mixed crystals Sb₂Se₃₋ₓTeₓ crystallizing in the Sb₂Te₃ structure type

As can be seen from Figure 26, for all investigated compositions the *a*- and *c*-lattice parameter decrease down to 50 K. Below this temperature, the lattice parameter show a slight increase. The relative temperature dependent change of the *a*-lattice parameter gets larger with increasing Se-content in the $Sb_2Se_xTe_{3-x}$ mixed crystals (Figure 30). The c-lattice parameter shows a more complicated behavior. The largest decrease as a function of temperature is observed for the most Se-rich composition.

However, the *c*-lattice parameter of the samples Sb_2Te_3, $Se_{0.6}Te_{2.4}$; $Sb_2Se_{1.2}Te_{1.8}$ show a nearly identical temperature dependence down to 50 K. Below this temperature the c-lattice parameter of $Sb_2Se_{1.2}Te_{1.8}$ stays almost constant, while it shows a significant increase for the other three compositions. The relative changes in the *a*- and *c*-lattice parameter are also reflected in the temperature dependence of the *c/a* ratio (Figure 28).

A comparison to literature data (Figure 28, 29 and 30) shows that the temperature dependence of the *a*- and *c*-lattice parameter as well as of the *c/a* ratio of Sb_2Te_3 determined in this study is in good agreement with the results published in the literature by [1], yet there are differences with respect to the data provided by [4] and [2]. These differences might be related to the different synthesis conditions, to systematic errors in the data, which cause an offset in the absolute value, or they could be related to differences in the chemical composition (no chemical analysis results were reported in the literature).

The *c/a* ratios of the $Sb_2Se_xTe_{3-x}$ mixed crystals within the stability field of the Sb_2Te_3 structure type increase with increasing Se contents (see Figure 28). In previous studies [Molodkin et al. [6]; Lostak et al. [8] it was proposed that Se is preferentially incorporated into the Te1 site of the Sb_2Te_3 crystal structure.The composition of the mixed crystals $Sb_2Se_{0.6}Te_{2.4}$, $Sb_2Se_{1.2}Te_{1.8}$ and $Sb_2Se_{1.8}Te_{1.2}$ would then represent different stages of the Se ordering and this could result in the different temperature dependence of the *c/a* ratios. In the structure of $Sb_2Se_{0.6}Te_{2.4}$ the Te1 site is partially occupied by Se, while the Te2 site is saturated completely with Te. The interactions between neighboring Te2 atoms are thus undisturbed by the Se incorporation. The incorporation of the smaller Se into the Te1 layers perpendicular to *c* in $Sb_2Se_{0.6}Te_{2.4}$, could lead to a larger relative shrinkage of the *a*-lattice parameter when compared to *c*- (see Table 15) and hence the *c/a* ratio of this compound is increased when compared to the one of Sb_2Te_3. In the crystal structures of $Sb_2Se_{1.2}Te_{1.8}$ and $Sb_2Se_{1.8}Te_{1.2}$ the Te1 site

is saturated completely by Se and in addition there is a small and a large excess of Se on the Te2 site, respectively. Thus for these two compositions also the Te2 layers incorporate the smaller Se ion leading to a stronger decrease of the *a*-lattice parameter when compared to the one of $Sb_2Se_{0.6}Te_{2.4}$, (see Table 15 and Figure 26). Hence, the *c/a* ratio of $Sb_2Se_{1.2}Te_{1.8}$ and $Sb_2Se_{1.8}Te_{1.2}$ is even larger than in $Sb_2Se_{0.6}Te_{2.4}$ (see Figure 28). The different behavior of the c lattice parameter of $Sb_2Se_{1.8}Te_{1.2}$ as a function of temperature (see Table 15 and Figure 27) could be directly related to the large excess of Se on the Te2 site, which should influence the Te…Te interactions. . Finally, the preferred incorporation of Se into one of the Te-sites might also be closely related to the non-ideal miscibility for the $Sb_2Se_xTe_{3-x}$ solid solution in the stability field of the trigonal phase (Figure 22), which was reported by Molodkin et al. [6]

5.2.2 Sb$_2$Se$_3$ structure

For Sb_2Se_3, all lattice parameters show a similar temperature dependency. The lattice parameters decrease in the temperature range from 300-50 K; below this temperature all three show a small increase. There are no indications of phase transitions in the measured temperature range.   The decrease in the *a*-lattice parameter with decreasing temperature is the smallest, the decrease in *c* is the largest. The relative change of the lattice parameter *b* and *c* is comparable down to about 150 K. Below 150 K the temperature-dependent changes of the lattice parameter *c* are larger with respect to the lattice parameter *b*.

6. Outlook

Several mixed crystals in the system $Sb_2Se_{3-x}Te_x$ were synthesized using various routes. Quantitative chemical analysis shows that the element concentrations of the mixed crystals deviate significantly from the expected compositions. Therefore, suitable reaction conditions to minimize the losses of Se during the synthesis should be further developed.

The lattice parameter of the $Sb_2Se_{3-x}Te_x$ mixed crystals as a function of the compositional parameter *x* and the temperature were investigated in detail in this thesis. Various anomalies in the thermal behavior of the lattice parameter and a deviation from Vegard´s law which indicates non ideal miscibility in the stability fields of the trigonal phase were found. These observations could be closely related to the preferred incorporation of Se into one of the two available Te sites in the crystal structure as already suggested by A.N.Mansour et al.[2] , A.K.Molodkin et al.[6]. In order to better understand the thermal expansion of the compounds and to unambiguously characterize the (dis)order of Se and Te, a detailed knowledge about the dependence of the atomic coordinates and displacement parameters of the atoms on the compositional parameter x and the temperature are desirable. For this, diffraction measurements on single crystals are warranted. These would also allow relating the observed variations to changes in individual interatomic distances and angles.

7.Acknowledgements

Bibliography

[1] D.Bessas, I.Sergueev, H.-C.Wille, J.Persson, D.Ebling and R.P.Hermann. Lattice dynamics in Bi_2Se_3 and Sb_2Te_3: Te and sb density of phonon states. *Physical Review* B, 86; 224301, (2012)

[2] A.N.Mansour, W.Wong, Q.Huang, W.Tang, A.Thompson and J.Sharp. Structural characterization of Bi_2Se_3 and Sb_2Te_3 as a function of temperature using neutron powder diffraction and extended X-ray absorption fine structure techniques. *Journal of Applied Physics*, 116; 083513, (2014)

[3] G.P.Voutsas, A.G.Papazoglou, P.J.Rentzeperis and D.Siapkas. The crystal structure of antymony selenide, Sb_2Se_3. *Zeitschrift Für Kristallographie,* 171; 261-268, (1985).

[4] X.Chen, H.D.Zhou, A.Kiswandhl, I. Miotkowski, Y.P.Chen, P. A.Sharma, A.L.Lima Sharma, M.A.Hekmaly, D.Smimov and Z.Jiang. Thermal expansion coefficients of Bi_2Se_3 and Sb_2Te_3 crystals from 10K to 270K. *Applied Physics Lettters*, 9; 261912, (2011).

[5] H.Liu, C.R.Knowles and L.L.Y.Chang. Exten of solid solution in Pb-Sb and Sb-Bi chalcogenides. *The Canadian Mineralogist*, 33; 115-128, (1995).

[6] A.K.Molodkin, V.I.Ivlieva, E.V.Meshcheryakova. Odering in $Sb_2Te_3 - Sb_2Se_3$ solid solution*. Zhurnal Neorganicheskoi Khimii,* 24; 176-182, (1979).

[7] E.P.Amaladass, T.R.Devidas, S.Sharma, C.S.Sundar, A.Mani and A.Bharath. Magneto-transport behaviour of $Bi_2Se_{3-x}Te_x$: role of disorder. *Journal of Physics: Condens Matter*, 28; 7, (2016).

[8] P.Lostak, R.Novotny, J.Horak. Effect of bond polarity in $Sb_2Te_{3-x}Se_x$ single crystals. *Czechoslovak Journal of Physics,* B; 39, (1989).

[9] D.P.Gosain, T.Shimizu, M.Ohmura, M.Suzuki, T.Bando and S.Okano. Some properties of $Sb_2Te_{3-x}Se_x$ for nonvolatile memory based on phase transition. *Journal of materials science,* 26; 3271-3274, (1991).

[10] S.S.Garje, D.J.Eisler, J.S.Ritch, M.Afzaal, P.O'Brien and T.Chivers**.** A New Route to Antimony Telluride Nanoplates from a Single-Source Precursor**.** *Journal of American Society.* 128; 3120–3121, (2006).

[11] Gajendra Gupta and Jinkwon Kim. Facile synthesis of hexagonal Sb_2Te_3 nanoplates using Ph$_2$SbTe*R* (*R* = Et, Ph) single source precursors . *Dalton Transactions,* 42; 8209-8211, (2013).

[12] A.S.Pashinkin, A.S.Malkova, M.S.Mikhailova. The Heat Capacity of Solid Antimony Selenide. *Russian Journal of Physical Chemistry*, 82; 1035–1036, (2008).

[13] A.F.Holleman and E.Wiberg. Lehrbuch der Anorganischen Chemie. 103. ED. *Walter de Gruyter,* (2007).

[14] R.Allmann. Röntgenpulverdiffraktometrie. 2.ED. *Springer,* (2002)

[15] http://www.ammrf.org.an

[16] http://pd.chem.ucl.ac.uk

[17] www.xhuber.de

[18] http://www.doitpoms.ac.uk

[19] D.H.Le Bail, A. And J.L.Fourquet. Ab-initio Structure determination of $LiSbWO_6$ by X-Ray powder diffraction. *Materials Research Bulletin*, 23; 447-452, (1988).

[20] L,Palatinus,V.Petricek and M.Dusek. Jana2006-the crystallographic computing system. *Acdemy of Science of the Czech Republic,Praha,* (2006).

Attachment

[Table A] Details on the synthesis of the samples

Sample		Sb_2Te_3	$Sb_2Se_{0.6}Te_{2.4}$	$Sb_2Se_{1.2}Te_{1.8}$	$Sb_2Se_{1.8}Te_{1.2}$	Sb_2Se_3
Amount	Sb	0.01600	0.01676	0.0176	0.0186	0.0208
/ mol	Se	0	0.005028	0.01056	0.0167	0.0312
	Te	0.024	0.020112	0.01584	0.01116	0
Molar.	Sb	121.7	121.7	121.7	121.7	121.7
mass	Se	78.971	78.971	78.971	78.971	78.971
g/ mol	Te	127.60	127.60	127.60	127.60	127.60
Theo.	Sb	1.948(1.947)	2.0405(2.0427)	2.1428(2.1479)	2.2646(2.2677)	2.5324
Mass	Se	0	0.3971(0.3975)	0.8339(0.8359)	1.3220(1.3239)	2.4645
/ g	Te	3.0624	2.5663	2.0212	1.4240	0
Weight	Sb	1.947	2.041	2.142	2.269	2.533
/ g	Se	0	0.399	0.836	1.325	2.465
	Te	3.061	2.569	2.026	1.426	0

[Table B]

Step	background	shift	Lattice parameter (a,b,c)	Gw	Gu	Lx	100 cycles	Bera's correction
1	x	AVG	x	x	x	x	x	
2	x	AVG	x	x	x	x	x	x